TECHNISCHE UNIVERSITÄT WIEN

DIPLOMARBEIT

Quantifying Vegetation Change in Drained Thermokarst Lake Basins using Remote Sensing

zur Erlangung des akademischen Grades

Diplom-Ingenieur

im Rahmen des Studiums

Masterstudium Geodäsie

eingereicht von

Clemens von Baeckmann
Martrikelnummer 01101834

ausgeführt am Institut für Geodäsie und Geoinformation
der Fakultät für Mathematik und Geoinformation
der Technischen Universität Wien

Betreuerin: Privatdoz.in Dipl.-Geografin Dr.in Annett Bartsch

Wien, 05.12.2023

(Unterschrift Verfasser) (Unterschrift Betreuerin)

Abstract

Arctic permafrost landscapes are in rapid transition and strongly affected by climate warming. Remote sensing methods can help for a better understanding and monitoring of those landcover changes. Common features of arctic permafrost landscapes are thermokarst lakes and drained lake basins. They play an important role for the geomorphological, hydrological and the ecological development of arctic landscapes. The change of habitat characteristics of arctic permafrost lowlands also effects the local biodiversity. Deepening our understanding of processes associated with drainage events and drained basins in the arctic environment is crucial for numerous applications (e.g., landscape models).

The study area is located on the Yamal peninsula in Northern Russia, Siberia. The peninsula can be categorized into a discontinuous and continuous permafrost tundra region. Yamal is covered by different tundra vegetation communities, thaw lakes, wetlands and river floodplains. Drained lake basins differ between the regions in their frequency of occurrence and in their size. We selected several drained lake basins on the Yamal peninsula representing a North-South climatic gradient and different drained lake basin development stages. Some drained lake basins are close to infrastructure. Human activity on Yamal does comprise not only gas infrastructure projects but extensive reindeer herding serves as main traditional land use form.

Drained lake basins and associated landscape dynamics such as changes in surface water area and vegetation cover can be monitored from space and described with different remote sensing indices. The different indices can be calculated from multiple satellite images on an annual and inter-annual level. In detail, the selected drained lake basins are evaluated at the peak of the growing season (between July 1. and August 31.) and inter-annual landcover dynamics from 2016 up to present. For this thesis multispectral imagery data was used, which was received from Sentinel-2 and Landsat-8 satellites. The derived data was used to calculate a range of different landcover metrics such as Normalized Difference Vegetation Index (NDVI) and Tasseled Cap (TC) indices. The Tasseled Cap coefficients were adjusted to the corresponding satellite and the spectral indicators for brightness, greenness and wetness were calculated.

The results were analysed by comparing the different sites, focusing on the connection of the studied parameters and site-specific factors (such as relative basin age, hydrological connectivity). In addition, comparisons are made to a landcover classifications developed within the ESA DUE Globpermafrost and Permafrost cci projects which are based on fusion of Sentinel-1 and 2 data using machine learning. The results will advance the understanding of drained lakes greening and the corresponding change of flora and fauna and biodiversity.

Kurzfassung

Die arktischen Permafrostgebiete befinden sich in einem schnellen Wandel und sind stark von der Klimaveränderung betroffen. Methoden der Fernerkundung können dabei helfen, diese Landbedeckungsveränderungen besser zu verstehen und zu überwachen. Gemeinsame Merkmale arktischer Permafrostgebiete sind Thermokarstseen und verschwindene Seen. Sie spielen eine wichtige Rolle für die geomorphologische, hydrologische und ökologische Entwicklung arktischer Gebiete. Die Veränderung des Lebensraumes wirkt sich auch auf die lokale Artenvielfalt aus. Die Vertiefung unseres Verständnisses der Prozesse im Zusammenhang mit Entwässerungsereignissen und entwässerten Einzugsgebieten in der arktischen Umwelt ist für zahlreiche Anwendungen (z. B. Landschaftsmodelle) von entscheidender Bedeutung. Diese Arbeit fokusiert auf das Gebiet der Halbinsel Jamal im Norden Russlands, Sibirien. Jamal wird in eine diskontinuierliche und eine kontinuierliche Permafrost-Tundra-Region eingeteilt werden. Jamal ist von verschiedenen Tundra-Vegetationsgemeinschaften, Tauwasserseen, Feuchtgebieten und Flussauen bedeckt. Entwässerte Tauseebecken unterscheiden sich zwischen den Regionen in ihrer Häufigkeit und Größe. Für diese Arbeit wurden mehrere entwässerte Seebecken auf der Jamal-Halbinsel manuell ausgewählt. Dabei wurde ein Nord-Süd-Klimagradient und verschiedene Entwicklungsstadien der entwässerten Seebecken berücksichtigt. Einige trockengelegte Seebecken liegen in der Nähe von Infrastruktur. Menschliche Aktivitäten auf Jamal umfassen nicht nur Gasinfrastrukturprojekte, sondern auch die Rentierhaltung dient als wichtigste traditionelle Landnutzungsform. Entwässerte Seebecken und damit verbundene Landschaftsdynamiken wie Veränderungen der Oberflächenwasserfläche und der Vegetationsbedeckung können aus dem Weltraum überwacht und mit verschiedenen Fernerkundungsindizes beschrieben werden. Die Indizes können aus mehreren Satellitenbildern auf Jahres- und Zwischenjahresebene berechnet werden. Im Detail werden die ausgewählten entwässerten Seebecken auf dem Höhepunkt der Vegetationsperiode (zwischen dem 1. Juli und dem 31. August) und der zwischenjährlichen Landbedeckungsdynamik von 2016 bis heute bewertet. In dieser Arbeit werden multispektrale Bilddaten von Sentinel-2- und Landsat-8-Satelliten verwendet und eine Reihe verschiedener Landbedeckungsmetriken berechnet, wie z. B. den Normalized Difference Vegetation Index (NDVI) und die Tasseled Cap (TC) - Indizes. Die TC Indizes wurden an den entsprechenden Satelliten angepasst und die spektralen Indikatoren für "Brightness", "Greenness" und "Wetness" berechnet.

Die Ergebnisse wurden verglichen anhand der verschiedenen Standorte, wobei der Schwerpunkt auf standortspezifischen Faktoren (wie relatives Beckenalter, hydrologische Konnektivität) lag. Darüber hinaus wurden Vergleiche mit Landbedeckungsklassifizierungen durchgeführt, die im Rahmen der ESA-Projekte DUE Globbermafrost und Permafrost cci entwickelt wurden und auf der Fusion von Sentinel-1- und 2-Daten mithilfe maschinellen Lernens basieren. Diese Ergebnisse sollen helfen das Verständnis der Begrünung entwässerter Seen und der damit verbundenen Veränderung von Flora und Fauna und der einhergehenden Änderung von Biodiversität vorantreiben.

Acknowledgements

I want to thank my supervisor Dr. Annett Bartsch for giving me the opportunity to work and study at her company b.geos. Also I want to highlight the important inputs from Helena Bergstedt at any time. Thanks for the enriching time with the colleagues at work. I also want to thank my family for their support and trust.

Contents

List of Acronyms

AL	Active Layer	22
ALT	Active Layer Thickness	20
BOA	Bottom of Atmosphere	12
CAL	Circumpolar Arctic Landcover	38
CALC-2020	Circumpolar Arctic Land Cover 2020	33
CALU	Circumpolar Arctic Landcover Units	12
CAVM	Circumpolar Arctic Vegetation Map	33
CCI-LC	Climate Change Initiative - Land Cover	33
C3S	Climate Change Service	40
CDS	Climate Data Store	40
DLB	Drained Lake Basin	12
DLBs	Drained Lake Basins	11
ECMWF	European Centre for Medium-Range Weather Forecasts	40
ERA5	ECMWF Re Analysis in the fifth generation	12
EU	European Union	29
EO	Earth Observation	29
EM	Electromagnetic	11
ESA	European Space Agency	29
ESRI	Environmental Systems Research Institute	11
GRIB	GRIdded Binary or General Regularly-distributed Information in Binary form	40
VH	Vertical transmitted and horizontal received	30
IPCC	Intergovernmental Panel on Climate Change	15
IW	Interferometric Wide	49

List of Figures

List of Tables

Chapter 1

Introduction

1.1 Motivation

The arctic is warming four times faster then the rest of the globe (Rantanen et al., 2022). Most of these regions are underlined by Permafrost (Obu et al., 2021) which is frozen ground for more then two consecutive years (French, 2007) and the Arctic tundra is covered in snow for up to 10 months of the year (Olsson et al., 2003). The Representative Concentration Pathway (RCP) 4.5 scenario developed within the Intergovernmental Panel on Climate Change (IPCC) highlights that permafrost thaw will affect more than 1200 settlements, 36.000 buildings, 69 percent of infrastructure in the pan-arctic, and 4 million people in Europe for the year 2050 (IPCC, 2022). Those landscapes related to permafrost are in rapid transition circumpolar and therefore strongly affected by climate warming (Vincent et al., 2017). The authors Schuur et al. (2022) mention that we should be considering a "country of permafrost" when we design human emission targets to stabilize global warming in a future warmer world. This highlights that the impacts of this polar transition extend to the entire planet (Meredith et al., 2022).

Research regarding earths climate must be conducted very precise, especially if changes in the system are irreversible. The IPCC evaluates the permafrost as a key tipping element (Lenton et al., 2008) which is a large-scale component of the earth system that may pass a tipping point (the threshold at which a system changes irreversibly) (Lenton et al., 2008). This changing climate influences also plants, animals, and other organisms that interact with the transition of the state of permafrost (French, 2007) resulting in drastic impacts on permafrost dynamics, ecosystem functioning, biogeochemical processes, and human livelihoods in lowland permafrost regions (Jones et al., 2022). In Figure 1.1 different observational datasets are averaged and show the temperature trend for the Arctic region. Circumpolar landscapes were traditionally seen as carbon sink but developed into carbon source areas through the ongoing thawing of permafrost (IPCC, 2022).

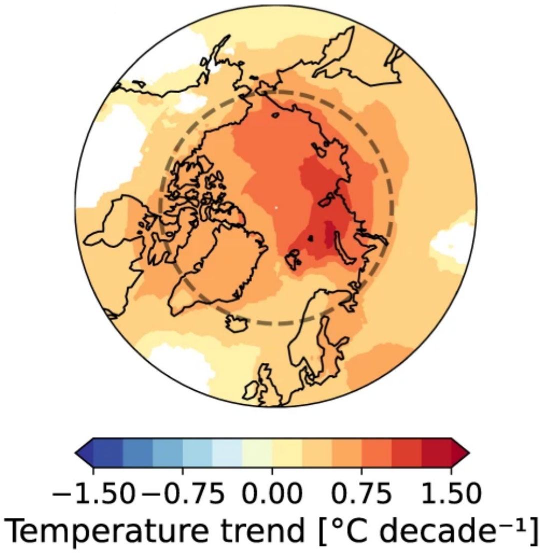

FIGURE 1.1: Temperature trend for the annual mean for 1979–2021. Areas without a statistically significant change are masked out, Figure adopted from Rantanen et al. (2022).

About 1,460 to 1,600 Petagram of organic carbon (Pg C) are stored in the northern circumpolar permafrost region alone. This is nearly twice the amount of carbon than the carbon present in the atmosphere (Schuur et al., 2022). Data from geological records showed that gradual change in one component can lead to sudden changes in the Earth system (Brovkin et al., 2021). Increased by the greenhouse effect of this released carbon dioxide and methane into air, permafrost is seen as an essential climate variable and associated with climate tipping points (Bartsch et al., 2023b).

Common features of permafrost landscapes are thermokarst lakes and DLBs, which play an important role for the geomorphological, hydrological and the ecological development of Arctic landscapes (Jones et al., 2022). The forming of those characteristic thermokarst landforms can be described as a process of the disturbance of the thermal equilibrium of the ground (Jones et al., 2011). The typical terrain of this topography influenced by the change in temperature is shown in Figure 1.2. Those lakes have a strong impact on carbon, energy and water fluxes and can be quite responsive to climate change (Nitze et al., 2017).

FIGURE 1.2: Thermokarst lakes in terrain underlined by permafrost. Visible is also the hydrological connectivity for different open water bodies describing an important site-specific factor. Photo was taken on Yamal, Siberia, on the 15$^{\text{th}}$ of August in 2015 by Annett Bartsch.

Several recent studies (Jones et al., 2022, Lara and Chipman, 2021, Nitze, 2018, Webb et al., 2022) have documented lake dynamics, and in particular lake drainage across lowland permafrost regions with implications for local, regional and global scale feedback. Significant changes in land-surfaces are observable *via* remote sensing, landscape dynamics can be detected and variables identified for characterizing the permafrost state changes (Lenton et al., 2008). Those landcover changes related to lake drainage events affect the carbon cycle and induce habitat changes that disturb the local biodiversity. For example glacier mass loss, permafrost thaw and decline in snow cover are projected to continue beyond the 21st century (high confidence) (IPCC, 2022).

There are numerous applications (e.g., landscape models, carbon cycle processes and local infrastructure stability) which depend on parameters describing the Arctic environment associated with permafrost conditions and surrounding terrain.

1.2 Objectives

The main objective of this thesis is to detect and describe the greening process of vegetation in DLBs using remote sensing techniques. Further more knowledge is established on specific patterns of the change in DLBs.

Impacts of lake drainage on local ecosystems through quantification of landcover changes following drainage events are monitored. This monitoring is needed to quantify the impacts of permafrost thaw on the carbon cycle, advancement in wetland and atmospheric greenhouse gas concentration (Bartsch et al., 2023b).

Chapter 2

Fundamentals

This chapter describes the fundamentals of Permafrost in Section 2.1 and important parameters in combination with permafrost: the Active Layer Thickness (ALT), the phenomena of the Talik, as well as the differentiation of Thermokarst and Non-Thermokarst lakes. Forming and draining of DLBs are described in 2.2, the Fundamentals of the remote sensing method is presented in Section 2.3 including different satellite sensors, derived Indices from satellites and the atmosphere influence.

2.1 Permafrost

Permafrost describes a frozen layer below Earth's surface. This ground remains at, or below 0 Degree Celsius for at least two continuing years. Permafrost is therefore a special thermal state of subsurface ground which can reach a vertical component of more than hundred meters (French, 2007). The ground of gravel, soil and sand is bound together with ice (Rutledge et al., 2023). More than 20 percent of the land-surfaces in the Northern Hemisphere's is underlined by permafrost at the present state (French, 2007) with a decreasing trend (Smith et al., 2022). Romanovsky et al. (2010) showed that the average thawing depth has increased by around 0.20 meters annually over a period of three decades.

A special type of this frozen ground phenomenon is permafrost which is located below the sea floor. This is so called sub-sea permafrost. Paull et al. (2022) showed that there are rapid seafloor changes associated with the degradation of Arctic submarine permafrost. Typical landform for a permafrost region is the tundra (no trees), but in the taiga (trees) there can be permafrost to some extend (Jorgenson et al., 2010), also in the alps, in high mountains some permafrost can be found. An example of permafrost is shown in Figure 2.1.

FIGURE 2.1: Permafrost ground ice expanding and destroying vegetation cover above. In the center, right, a measuring stick (20 cm) is clearly visible. Photo was taken between Inuvik and Tuktoyaktuk, Nordwest-Territorien, Canada on the 20$^{\text{th}}$ July 2023, by Clemens von Baeckmann.

The distribution of Permafrost in the Arctic is not uniform. There is a clear variability in the extent of permafrost for example in North America and North Eurasia. In the Figure 2.2 the extend of the permafrost (Obu et al., 2021) and infrastructure (Bartsch et al., 2021) for the Arctic region is shown.

In some regions the infrastructure is on high risk due to the thawing of the permafrost by mid-century (Hjort et al., 2018, 2022, van der Sluijs et al., 2018). About 70 % of the build infrastructure on permafrost ground is located in areas with high potential for thaw of near-surface permafrost (Hjort et al., 2018). The authors Tanguy et al. (2023) showed that due to permafrost degradation 38% of the ponds at the surface are induced by human activity in their study area in Paulatuk, Canada. The anthropogenic warming causes an continuing of infrastructure damage, which will influence 30-50 % of critical circumpolar infrastructure till 2050 (Hjort et al., 2022).

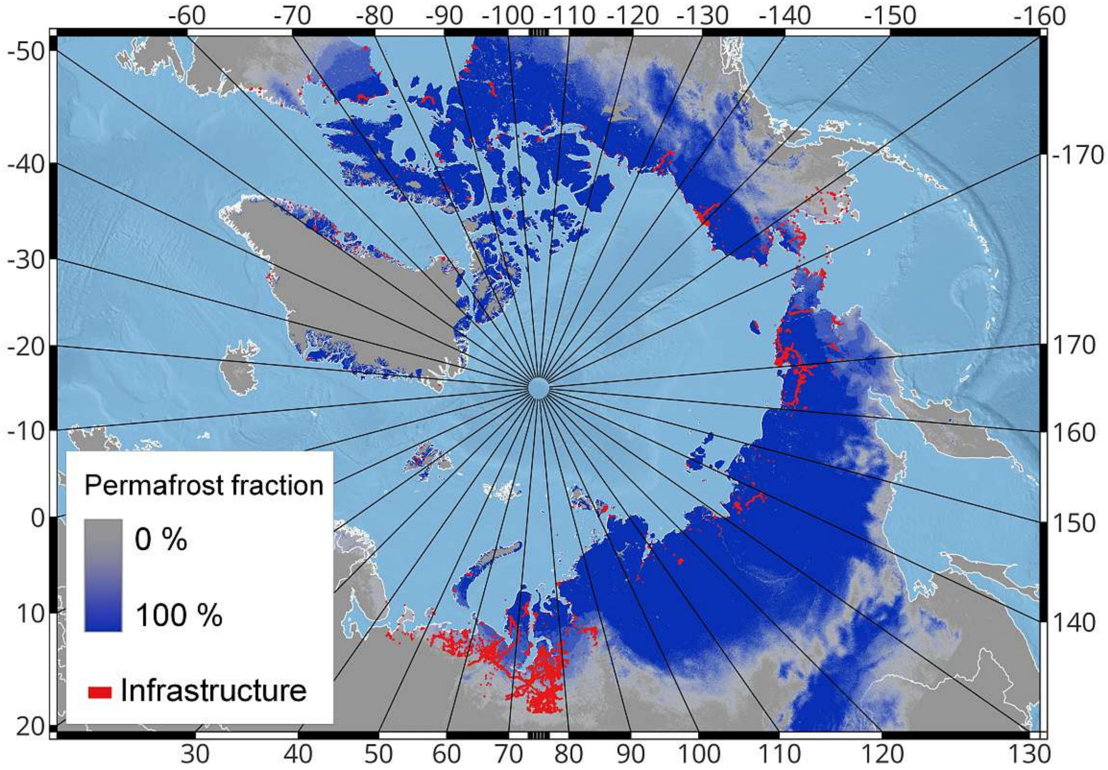

FIGURE 2.2: Permafrost extend Obu et al. (2021) and infrastructure data (red) Bartsch et al. (2021) for the Artic. Background layer: Ocean Bottom from the Natural Earth map data and the ESRI World Countries map.

Permafrost is given in fraction, in the traditional form it was separated into different classes (Brown et al., 1997). The classes and the corresponding fraction is shown in Table 2.1.

TABLE 2.1: Traditional Permafrost classes and corresponding fraction values

Class	**Fraction**
Continuous	90 - 100 %
Discontinuous	50 - 90 %
Sporadic	10 - 50 %
Isolated	up to 10 %

The Active Layer (AL) is used to characterize an important part of the permafrost state. There can be seasonally-frozen ground on the top of the permafrost, the so called active layer (French, 2007). This surface layer of ground is subject to annual thawing (during the summer) and freezing (during the winter) (Dobiński, 2020). Dynamics associated with the change in the AL are needed for better understanding permafrost degradation (Li et al., 2022). One of the most common measurements of the AL is the thickness and its change over time of it (Dobiński, 2020). One simple form to measure the depth of the AL is measuring it with using a ground penetrating stick till it reaches the frozen permafrost. Another form is data derived from borehole data (well log). Those indicate that the ALT reaches from 20 cm to more than 100 cm thickness (Osterkamp and Payne, 1981). The thickness is influenced not only by the season but also from the thickness of the surficial organic material, the thermal conductivity of the soil and the snow thickness distribution (Bergstedt et al., 2021). This is because snow has an insulating effect and preserves the heat stored in the ground in winter (Zhang, 2005). Changes in the snowcover due to changes in precipitation and temperature can influence the thickness of the active layer (Shur et al., 2011). Leibman et al. (2015) highlighted that spatial distribution of active layer depth depends on lithology of the rocks and surface cover but temporal changes are controlled by summer air temperature, summer precipitation and ground temperature.

The talik is a layer of unfrozen ground that occurs in permafrost areas due to an anomaly in thermal, hydrologic, or hydrochemical conditions (Schubert, 2015). This can for example be a lake, or even a large river located in permafrost regions (Parsekian et al., 2013). It is an important mechanism of permafrost degradation (Farquharson et al., 2022). The sub lake ground remains unfrozen the whole year (Jones et al., 2022). Sub wildfire ground and forest ground can form a talik (Farquharson et al., 2022) too. Due to climate change the talik is growing and they are predicted to reach a thickness of 12 m in areas of spruce forest by 2090 (Farquharson et al., 2022). Obu et al. (2021) highlighted that the talik can be affected by seasonal freezing and therefore they distinguish between:

- closed,
- open,
- isolated,
- lateral and
- transient talik.

Most active in methane production is the zone at the boundary of the talik (Kessler et al., 2012, Parsekian et al., 2013). To evaluate the potential of this sub lake methane production knowledge about the size and orientation is needed (Parsekian et al., 2013).

Thermokarst lakes are commonly known as shallow water-filled depressions (Kanevskiy et al., 2013). Those lakes can expand by the thermokarst induced processes like surface subsidence caused by the melting of massive ground ice and may freeze solid in winter (van Everdingen, 1998) (Manasypov et al., 2022). The lake basins typically undergo multiple stages of evolution (as shown below). Lake dynamics associated with permafrost thawing can include drainage, which effects local ecosystems and strongly influences the local biodiversity (Jones et al., 2022). There are two stages of evolution of lowland Arctic landscapes;

- primary, the lake formation and permafrost degradation and
- secondary, the lake drainage and permafrost aggradation (Jones et al., 2022).

Most of the thermokarst lakes formed about 11.000 years before present in the geological epoch called Holocene, when the Last Glacial Period ended and post glacial climate warming began. Those lakes are seen as result of local permafrost degradation in earths history. Erosional processes and thermokarst lakes are very dynamic features in Arctic and sub-Arctic lowland landscapes. Thermokarst lake change results in lateral and vertical dynamics which are triggered by the complex interactions with topography, streams, neighboring thermokarst lakes, and permafrost (Jones et al., 2011).

Typical grass and grass-like flowering plants from the taxonomic order *Poales* around and close to a thermokarst lake is shown in Figure 2.3. Not visible but present below the water is the so called Talik.

FIGURE 2.3: A Thermokarst Lake. Vegetation: *Cyperaceae (Eriophorum)* and closer to the water body *Poaceae*. Both are from the taxonomic order *Poales*. Photo was taken on the Yamal Peninsula, Siberia on the 26$^{\text{th}}$ July 2016, by Dorothee Ehrich.

Not surprisingly, these landscapes are highly vulnerable to permafrost thawing caused by anthropogenic climate change as we face now. The very important role those lakes have is their influence on the carbon cycle. They are transporting soil carbon to the hydrological network and the atmosphere. This phenomenon can be detected and monitored. Furthermore, a decrease in the organic carbon concentration was detected in lakes originated in lower permafrost fraction areas (taiga biome) to areas with higher permafrost fraction (tundra) (Manasypov et al., 2022).

Compared to the thawing of ice-rich permafrost there are also lakes in ice-poor permafrost terrain, so called Non-thermokarst lakes (Bergstedt et al., 2021, Jones et al., 2022). They develop when the natural input and output of the local water system permits the water to cumulate in those topographic depressions. Mostly those are in areas with coarse-grained sediments, such as sand and gravels, meaning they are thaw-independent basins. Often they have been preconditioned through fluvial, mass-wasting and aeolian processes that promote the pooling of water. The degradation of the permafrost below the lake is only minimal in ice-poor permafrost terrain (Jones et al., 2022).

2.2 Drained Lake Basins

The secondary stage of evolution of lowland Arctic landscapes results in so called DLBs caused by lake drainage and permafrost aggradation. The cause of drainage is a target of recent research and focus is set on specific external or internal processes. However, already in August 1979 research was conducted on Richards Island *(Canada)* in the Mackenzie delta area. Lake Illisarvik was artificially drained to investigate the change of the permafrost (French, 2007). In general; Lateral and internal drainage are the two distinct categories for the drainage process which are identified and related to the degradation of enclosing permafrost;

- The lateral thermokarst lake drainage has been frequently described for a number of regions in the circumpolar arctic areas in continuous permafrost regions (90 - 100 percent fraction). Bank overflow, ice wedge degradation and development of a drainage network, headward stream erosion, lake tapping, coastal erosion, as well as expansion of a lake toward a drainage gradient are detected causes for a drainage event.
- The internal drainage is usually documented in the zone of discontinuous permafrost ($<$ 90 percent fraction). Subsurface drainage is caused when the talik or a thawed zone beneath a lake penetrates the permafrost.

The two ways of drainage indicate that there is a huge diversity in extent and rate of the drainage, both influenced by climatic changes. This fact underlines how important it is to determine the causal mechanism for lake drainage in different regions (Jones et al., 2011). Jorgenson and Shur (2007) also mention that the base levels of the lakes are lowered progressively by the eroding of the outlet channels. E.g. see Figure 6.3 focusing on drainage channels.

As shown in Figure 2.3, the presence of vegetation around the lake is common and further colonizes a recently drained lake.

> "After lake drainage, DLBs become sites of plant colonization, peat accumulation, and permafrost aggradation and critical areas for carbon sequestration. Regionally, DLBs create a unique mosaic of tundra habitats characterized by various stages of post-drainage succession and diverse plant communities" Bergstedt et al. (2021).

Open water bodies can remain at the bottom of the basin or a part can refill the depression of the former lake. This reoccupied water can be separated into two fundamental types of water bodies:

- deeper and larger lakes created by thawing of the organic- and ice-rich materials in the center and
- small and shallow infilling ponds caused by impoundment of water in the low-lying margins of the basin (Jorgenson and Shur, 2007).

2.3 State of the art of permafrost monitoring

Satellite Remote Sensing (SRS) technology provides spatial and temporal accuracy over an extreme remote and vast area like the arctic regions. This characteristic serves as a supplementary component to field measurements and has the potential to fill in data gaps, as demonstrated by numerous studies (Bartsch et al., 2023b, Bergstedt et al., 2021, Jones et al., 2023, Jorgenson et al., 2010, Runge et al., 2022, Thies and Bendix, 2011, Wang et al., 2023, Widhalm et al., 2016, Zhao et al., 2023).

Valuable and unique insights can be provided by remote sensing. For example gaining a thorough quantitative comprehension of permafrost-related dynamics and their broader impacts extending beyond the local plot-scale from field work is possible. But the capabilities of remote sensing are restricted to surface measurements.

Remote sensing, (while unable to penetrate the ground and directly observe permafrost due to its nature as a subsurface phenomenon determined solely by ground temperature) can provide estimations on the distribution, magnitude, and impact of permafrost thaw.

This is achieved by detecting landforms and processes associated with the melting of excess ground ice (Bartsch et al., 2023b).

Problematic are the short periods of observation series and their corresponding uncertainties for capturing robust long term trends for climate variables (Yang et al., 2013). Another problem is that the measured data of surface radiance from a spacecraft in orbit is different compared to the ground surface radiance due to the Earth's atmosphere, which acts as a dispersive medium (Ueno and Mukai, 1977). The accuracy of the measured data can be improved by applying radiometric corrections to address the atmospheric effects to some extend but problems can still occur. In order to measure surface parameters, clouds, for example, represent a barrier that cannot be overcome with an Multi Spectral Instrument (MSI) because it can not penetrate water vapour. For example: the satellite Landsat-8 or Sentinel-2 has an MSI on board. On the other hand, a Synthetic Aperture Radar (SAR) which is on board the Sentinel-1 Satellite can penetrate water vapour.

- **Synthetic Aperture Radar (SAR)**
  SAR is a type of active microwave remote sensing that captures a high-resolution radar image from space (Moreira et al., 2013, Richards, 2009). Electromagnetic waves are emitted and the returning signal measured. Compared to normal radar measurements, which transmits signals in the nadir direction, a SAR system directs radar pulses to the side. The incidence angle is the angle at which the electromagnetic wave hits the earth's surface. The benefit of this side-view principle is that it allows the sensor to receive signals from various objects on Earth at different times, enabling the differentiation between these objects. The incidence angel is influenced by surface properties. For example the side of a mountain facing the sensor has a higher incidence angle than the corresponding side facing away (Jones and Vaughan, 2010). Shadows can occur as shown in the Figure 2.4. For example; a recent field of interest using SAR methods is subsidence measurements of permafrost (Bartsch et al., 2019a, Strozzi et al., 2018).

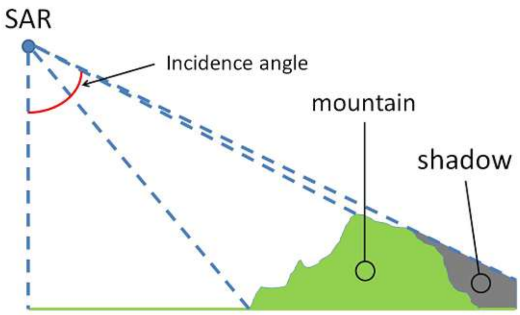

FIGURE 2.4: Radar shadow in mountainous areas. Schema adopted from Jones and Vaughan (2010).

The coefficient $\sigma 0$ is the measured backscatter. The scattering of the signals consist of surface scattering and volume scattering. Surface scattering occurs at a clearly defined boundary layer, while volume scattering occurs over a larger area. This is due to the large wavelength in relation to the objects detected, some of the energy penetrates the objects and is only then scattered back (Richards, 2009).

- **MultiSpectral Instrument (MSI)**

MSI is a passive type of remote sensing that captures a high-resolution image from space (Richards, 2009). Earth's reflected radiance is measured for different spectral bands, outreaching the RGB band as shown in Table 2.2. The derived data is used for computation of various remote sensing Indices describing the earths surface, for example the NDVI, Normalized Difference Moisture Index (NDMI) and the Normalized Difference Water Index (NDWI) (Nitze et al., 2018, Pahlevan et al., 2017). The atmosphere has an important role on different frequencies and therefore atmospheric corrections need to address atmospheric effects.

Atmospheric effects

Atmospheric effects are responsible for the discrepancy between the observed values from the satellite sensor and the ground surface radiance (Ueno et al., 1982, Ueno and Mukai, 1977). The atmospheric window describes the earths atmosphere characteristic on different frequencies.

For example 5 mm wavelengths are absorbed by the Oxygen molecule in the atmosphere (Pardo et al., 2001). For some frequencies the atmosphere is a so called dispersive medium as shown in the Figure 2.5. Visible light (400 - 650 nm) and microwaves (10 mm - 10 m) are less absorbed by the atmosphere and therefore they are inside the atmospheric window (Richards, 2009).

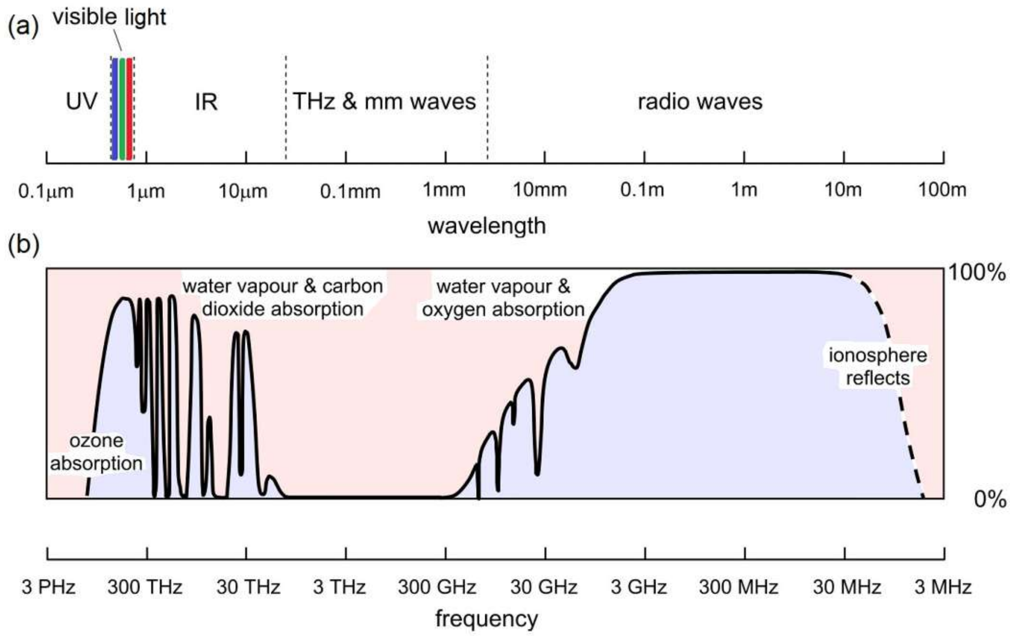

FIGURE 2.5: EM spectrum (a) and Earth's atmospheric opacity (b) for various wavelengths of the electromagnetic spectrum. In light red the absorbing effect and in light blue the atmospheric window, image modified from Richards (2009).

The European Space Agency (ESA) and the European Union (EU) run a space program called Copernicus which focus on Earth observation and provide data from satellite missions and *in-situ* data (ESA-Communications, 2011). One part of the Copernicus program is the Sentinel program, which replaces retired Earth Observation (EO) missions. Each of the satellite mission focuses on a different aspect of EO; Atmospheric, Oceanic, and Land monitoring (European Space Agency, 2022).

2.3.1 Satellite missions

There are different operational remote sensing satellites in space providing acquisition of satellite imagery of Earth. One of the oldest (1975) but still running program is the Landsat program, a joint National Aeronautics and Space Administration (NASA) and United States Geological Survey (USGS) program (Townshend and Short, 1984). The European pendant is the Copernicus Sentinel program. There are different satellite missions planned and operational:

- Sentinel-1, provides radar imaging for land and ocean services regardless of weather or time, day or night (applications: sea ice extend, subsidence in permafrost (Strozzi et al., 2018)).
- Sentinel-2, offers high-resolution optical imaging (MSI) at high spatial resolution (up to 10 meters), example application: NDVI change in DLBs (Chen et al., 2021).

- Sentinel-3, measures topography, temperature, marine ecosystems, water quality, pollution, and other features for ocean forecasting and global land monitoring services, permafrost related applications: land surface temp., snow modelling (Obu et al., 2021).
- Sentinel-4, will provide data for atmospheric composition monitoring (under construction), main focus is set on gas concentrations and aerosols in the atmosphere.
- Sentinel-5, provides data for atmospheric composition, with focus on air pollution using TROPOspheric Monitoring Instrument (TROPOMI) which is an ultraviolet, visible, near and short-wavelength infrared spectrometer, application: Methane anomaly detection in the arctic (Hachmeister et al. (2022) focused on Greenland).
- Sentinel-6, offers continuity in high precision altimetry sea level measurements using an radar altimeter. Possible permafrost related application: snow heights (Kern et al., 2020).

2.3.1.1 Sentinel-1

Sentinel-1 is a Low Earth Orbiting (LEO) satellite at an altitude of about 693 km, and offers day-and-night radar imaging using C-band SAR. There were two operational, polar-orbiting satellites, and planned missions:

- Sentinel-1A, launched on 3rd April 2014,
- Sentinel-1B, launched on 25th April 2016 - mission ended in 2021,
- Sentinel-1C and D are in construction.

The satellites provide all-weather imagery of earth's surface at 5.504 GHz. They are orbiting 180° apart, can achieve a six days revisiting period and fly at an altitude of about 700 km. Data across the Arctic are primarily acquired in Vertical polarization transmitted, Vertical polarization received (VV) and Vertical transmitted and horizontal received (VH) polarization (Bauer-Marschallinger et al., 2021) and thus are used for the analyses in this thesis. Data availability in recent years is however limited (for example the study region) due to the failure of Sentinel-1B in 2021.

A schematic view of the four different product modes for Sentinel-1 is shown in Figure 2.6.

- Interferometric Wide Swath (IW) mode records stripes at a resolution of 20 x 5 meter,

- Wave Mode (WV) provides intermittent bursts at a resolution of 5 x 5 meter (used for ocean records),
- Stripmap (SM) focuses on small ground view with high spatial accuracy (5 x 5 meter) compared to the
- Extra-Wide Swath (EW) mode which focuses on a broad ground coverage with less spatial resolution (20 x 40 meter).

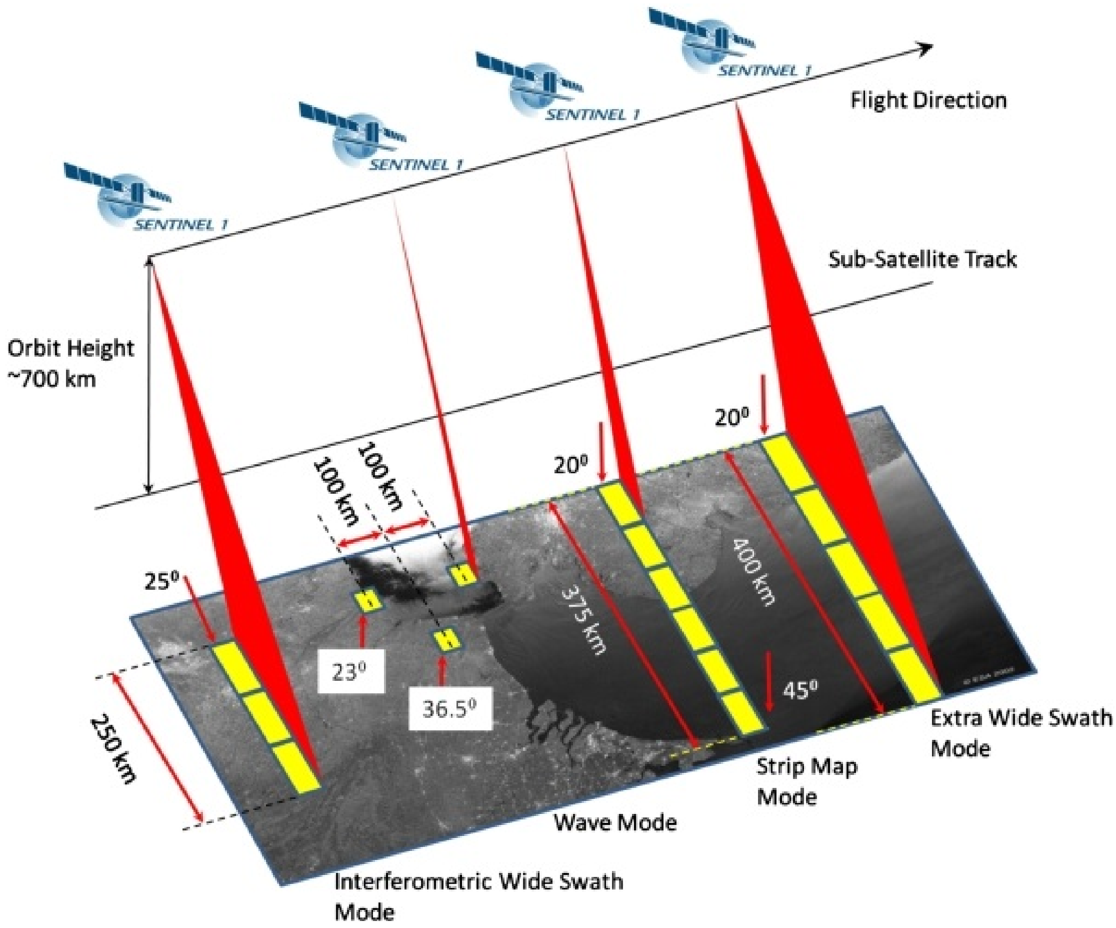

FIGURE 2.6: Four different acquisition modes are derived for Sentinel-1, image modified from European Space Agency (2022).

2.3.1.2 Sentinel-2

Sentinel-2 is an multispectral high-resolution imaging mission monitoring on 13 spectral bands including Short Wavelength Infrared (SWIR) and Near Infrared (NIR) bands. There are two operational, polar-orbiting satellites:

- Sentinel-2A, launched on 23th June 2015,

- Sentinel-2B, launched on 7$^{\text{th}}$ March 2017,
- Sentinel-2C, scheduled launch in 2024.

Both are two identical satellites in the same orbit, they provide a resolution up to 10 meter (depending on the spectral band see Table 2.2) and both satellites achieve a 5-day revisit period in combination.

The spectral brands differ for a small scale for each of the different satellites (2A/2B). The shown wavelength in the Table 2.2 is an approx.

TABLE 2.2: Sentinel-2 spectral bands and spatial resolution.

Band	**Wavelength [nm]**	**Spatial resolution [m]**	**additional Information**
B01	442	60	used for coastal aerosol detection
B02	492	10	"blue"
B03	559	10	"green"
B04	664	10	"red"
B05	704	20	Vegetation, red edge
B06	740	20	Vegetation, red edge
B07	780	20	Vegetation, red edge
B08	832	10	NIR
B8a	864	20	Narrow NIR
B09	945	60	Water vapour
B10	1375	60	SWIR, cirrus cloud detection
B11	1611	20	SWIR
B12	2200	20	SWIR

2.3.2 Indices

Different remote sensing indices were calculated:

- **NDVI**
  The NDVI index describes green proportions (relative biomass) (Tucker, 1979). The absorption by the chlorophyll pigments in the red band and the plant reflectance in the NIR band is used. The band data is used on BOA (Level 2A).

$$\frac{(B08 - B04)}{(B08 + B04)} \tag{2.1}$$

- **Tasseled Cap greenness**
  This index is used to describe vegetation. The band data is used on TOA (Level 1C).

$$TC_{green} = (-0.2848 * B02) - (0.2435 * B03) - (0.5436 * B04) + (0.7243 * B08) + (0.0840 * B11) - (0.1800 * B12) \tag{2.2}$$

- **Tasseled Cap wetness**
  This index describes interactions between soil and canopy moisture. The band data is used on TOA (Level 1C).

$$TC_{wet} = (0.1509 * B02) + (0.1973 * B03) + (0.3279 * B04) + (0.3406 * B08) - (0.7112 * B11) - (0.4572 * B12) \tag{2.3}$$

- **Tasseled Cap brightness**
  The index is used to describe soil properties. The band data is used on TOA (Level 1C).

$$TC_{bright} = (0.3037 * B02) + (0.2793 * B03) + (0.4743 * B04) + (0.5585 * B08) + (0.5082 * B10) + (0.1863 * B12) \tag{2.4}$$

2.3.3 Landcover

There are different data products which provide information about the landcover in the arctic, for example:

- CALU: Bartsch et al. (2023a) produced this landcover especially for tundra regions, spatial resolution is 10 m and 23 landcover units are distinguished.
- Climate Change Initiative - Land Cover (CCI-LC): lower spatial resolution compared to the CALU, also large differences in thematic content (especially the class forest seems to be overestimated because those areas are in the shrub tundra group of CALU)
- Circumpolar Arctic Vegetation Map (CAVM): Raynolds et al. (2019) generated a commonly known landcover product but have comparably low spatial detail (Bartsch et al., 2023a).
- Circumpolar Arctic Land Cover 2020 (CALC-2020): Liu et al. (2023b) derived their landcover across the entire terrestrial Arctic for circa 2020. It uses a combination of Sentinel-1/2 and digital elevation information. Analysis was made at 10

m spatial resolution and 10 landcover classes are distinguished. Compared to the CALU it has a lower thematic content (Bartsch et al., 2023a).

For this thesis the CALU landcover processing steps were used. One advantage is that it generates a transferable landcover and a consistent dataset (Bartsch et al., 2023a). Another advantage of the CALU is that it can be included in permafrost modelling, hydrology, and soil carbon up- scaling. This sensitiveness on wetland areas is shown in Figure 2.7. Another product where wetland areas are well visible is the CALC-2020 landcover by Liu et al. (2023b). This landcover shows the most detail on wetland areas but uses a classification driven by terrain information.

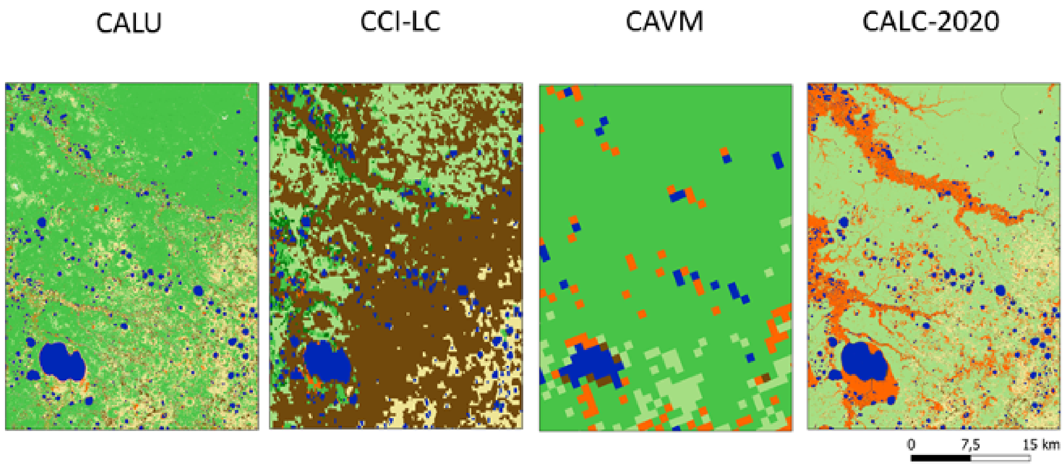

FIGURE 2.7: Comparing different landcover products. Single classes/units are grouped for comparison. For Legend see Table 4.1 Group A. Figure adopted, Bartsch et al. (2023a).

Chapter 3

Study area and data

3.1 The Yamal peninusla

The study area is located on the Yamal peninsula in Northern Russia, Siberia and extends to the amount of about 126 000 km^2. The distance for the north - south gradient is 780 km. The peninsula can be categorized into a discontinuous and continuous permafrost tundra region. Yamal is covered by different tundra vegetation communities, thaw lakes, wetlands and river floodplains. DLBs differ between the regions in the frequency of occurrence and in their size. Yamal is representing a north - south climatic gradient caused by the geographic orientation of the peninsula. We selected several DLBs on the North-South gradient and different basin development stages as shown in Figure 3.1 below.

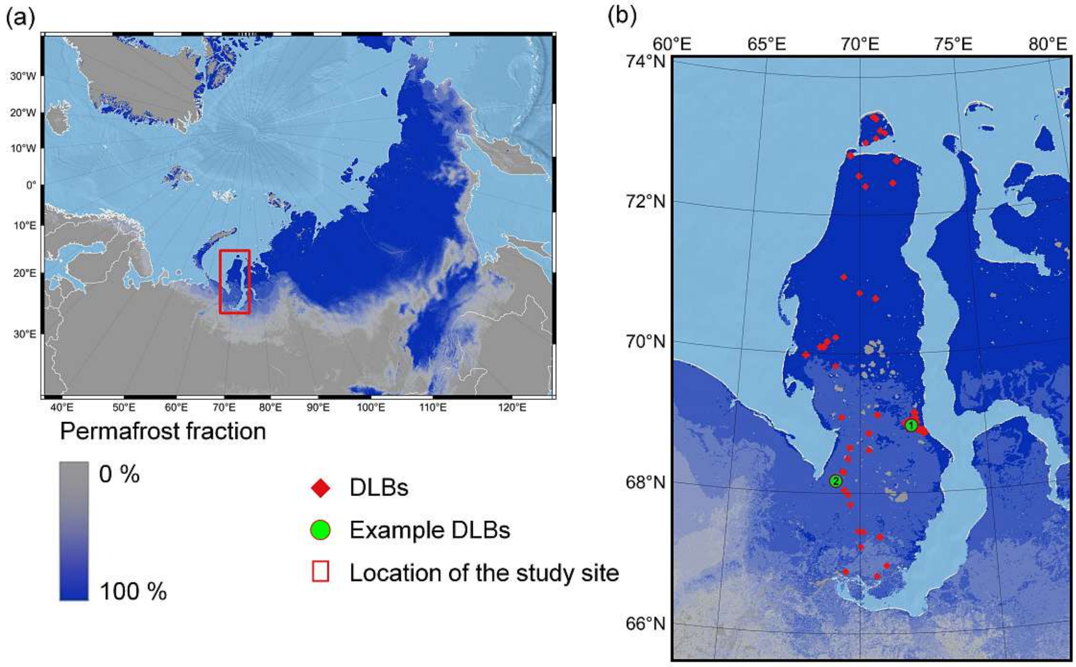

FIGURE 3.1: Location of the study area, on Yamal, Siberia. Overview of the location for the study site in (a) indicated with red rectangle and (b) the selected DLBs and the Examples 1 and 2 in the green circle. The background layer is the Ocean Bottom from the Natural Earth map data and the ESRI World Countries map. The permafrost fraction is derived from Obu et al. (2021) and the shape from the selected lakes are taken from the Nitze (2018) dataset.

There are shallow and smaller lakes present on Yamal. Those lakes have developed closed taliks below the bottom of the lake and reach a thickness of 5–7 m (Leibman et al., 2015). A typical landscape characteristic are wetlands, especially mires. Low erect shrub willow (Salix) is abundant in Yamal and cover the different valleys and slopes (Kumpula et al., 2012, Leibman et al., 2015).

The Vaskiny Dachi research station is located in the center of Yamal. This region is also home to one of the largest gas reserves in the world. To extract the gas and transport the equipment a railroad was built in 2010. This railroad is 572 km long and connects the city of Moscow *via* Obskaya to the Gas field Bovanenkovo. The train line is called the Obskaya–Bovanenkovo Line and owned and operated by Gazprom (Kumpula et al., 2012). Close to the Vaskiny Dachi research station extensive slope process activations are present which result in cryogenic landslides and are monitored since 1989 (Leibman et al., 2015). But also the animal live is influenced by this change. The fish population dropped during the building process of the gas infrastructure but returned after completion of river crossings of railways and roads in some cases (Kumpula et al., 2012).

Human activities on Yamal include not only gas infrastructure projects, but also extensive reindeer herding, which serves as the main traditional form of land use. Nomadic reindeer herders, Nenets, (Komi and Khanty families to a lower extend) move annually between winter pastures at the tree line (lower south of Yamal) and the northern tundra. This nomadic living exposes them to impacts associated with exploration and production activities (T. Kumpula and Stammler, 2010). The fauna on the Yamal peninsula experiences hard conditions additionally to strong temperature gradients from North to south as shown in Figure 3.3. There are more reindeers on Yamal then indigenous people, about 310 000 domestic reindeers and approximately 6 000 indigenous nomadic living people call the Yamal peninsula their home (Kumpula et al., 2012).

3.2 Data

3.2.1 Landcover data

Landcover data function as a base for upscaling of ecosystem characteristics in permafrost regions (Bartsch et al., 2019b). Those landcover data-sets are produced depending on the user requirements for example permafrost modelling, hydrology and soil carbon upscaling methods (Bartsch et al., 2019b). The used approach in this study generates Circumpolar Arctic Landcover (CAL) Units (Bartsch et al., 2023a) focusing on a broad data coverage across the Arctic permafrost regions. Most of the landcover products are static products with a high consistency over the spatial extend (example: (Bartsch et al., 2023a, Gong et al., 2012)) but this research focuses on a space-for-time concept on landcover change for selected DLBs. This requires the different dated landcover maps but also additional knowledge on the exact drainage date. An advantage of this research is that the landcover data produced only needs to be generated over a small spatial extent while Bartsch et al. (2023a) also needed complete cloud free data as input for the spatial coverage.

The average landcover distribution on the Yamal peninsula is derived *via* the CALU as shown in Figure 3.2. The various landcover units have a very heterogeneous distribution. The presence for the landcover unit is highest for #9 'dry to moist tundra, prostrate to low shrubs' and lowest for 'recently burned or flooded, partially barren' (#17). The low number of classified pixels for the unit 'forest' (#18) reflects the Yamal peninsula very well due to its location location above the tree line.

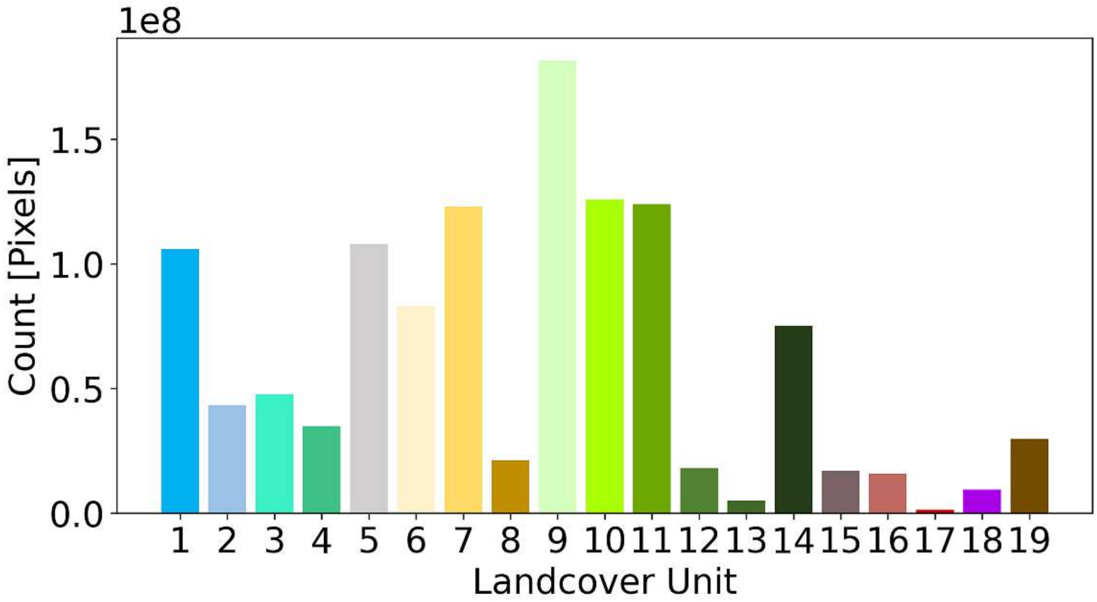

FIGURE 3.2: Average landcover distribution for the Yamal peninsula. The landcover Units follow the color scheme as presented in Table 4.1.

3.2.2 Lake change trend data

The extend for the selected lakes is derived *via* the trend dataset from Nitze et al. (2018). The polygons are adopted from the Hot Spot Regions of Permafrost Change ("Hot Spot Product") (Nitze, 2018). Those "Hot Spot Regions" were identified using different spectral indices. The TC for brightness, TC greenness and the TC for wetness were used as input data. Also the NDVI, the NDMI and the NDWI were used. These remote sensing indices provide valuable information about surface properties. For example: information about albedo values, vegetation presence or moisture/water presence are given for the surface (Nitze, 2018).

The basis for this dataset is provided by the Landsat satellite. The Landsat time-series stacks supplied by the USGS were used to derive those parameters but only data for the peak of the summer season was taken (July and August). Data for the years 1999 till 2014 were then used to calculate the trend parameters (slope and intercept) using the robust Theil-Sen regression algorithm.

This resulted in a dataset providing a resolution on a 30 x 30 meter scale for different regions around the Arctic. The final product extend over defined study regions: Western Siberia, Eastern Siberia, Alaska and Eastern Canada. For this study the region Western Siberia was used because it covers the whole Yamal Peninsula. The dataset was downloaded *via* PANGAEA, a Data Publisher for Earth and Environmental Science webpage. 218 882 different lakes are included in this database as geospatial vector file and contain the perimeters of maximum extent of individual lakes larger than one ha buffered by 30 meters (Nitze et al., 2018). For each of the lakes 14 different attributes were given (see Table 3.1).

TABLE 3.1: Attributes supplied by the trend dataset from Nitze et al. (2018).

Attribute	**Description**
ar_st_ha	area at start of observation (1999) in ha
ar_en_ha	area at end observation (2014) in ha
nt_ch_ha	Net lake area change in ha
nt_ch_pc	Net lake area change in ha
gr_gn_ha	Gross lake area gain in ha
gr_gn_pc	Gross lake area gain in percent
gr_ls_ha	Gross lake area loss in ha
gr_ls_pc	Gross lake area loss in percent
sw_ha	Stable water area in ha
pe_mt	Perimeter in meter
ec_rt	Eccentricity ratio
or_dg	Orientation in degree
so_rt	Solidity ratio

3.2.3 Meteorological records

Meteorological data for the Yamal peninsula is derived using the ERA5 Land-surface dataset. This dataset includes information on climate attributes for example temperature and precipitation and is a product produced by the Copernicus Climate Change Service (C3S) at the European Centre for Medium-Range Weather Forecasts (ECMWF). This fifth generation of atmospheric reanalysis data for global climate parameters covers a period from 1940 up to present. The principle of this data is a combination of observational data merged into a global dataset, producing data that is consistent over time (Hersbach et al., 2020). The Climate Data Store (CDS) portal provides the data for download. The data comes in the GRIdded Binary or General Regularly-distributed Information in Binary form (GRIB), a compact data format commonly used in meteorology. The Network Common Data Format (NetCDF) is available in experimental status alternatively.

Air temperature at two meters above the surface were used for the selection of Sentinel-1 scene observations (see Section 4.5) from the "ERA5 hourly data on single levels from

1940 to present" dataset because accurate information on land states were given. A high temporal and spatial resolutions of the ERA5-Land dataset is achieved. The spatial resolution is a 30 x 30 km grid in the horizontal. The vertical resolution includes 137 levels up to 80 km height (Hersbach et al., 2020), a full description is given in the Table 3.2.

TABLE 3.2: ERA5 dataset description.

Data type	Gridded
Projection	Regular latitude-longitude grid
Horizontal coverage	Global
Horizontal resolution	0.1° x 0.1°, Native resolution is 9 km.
Vertical coverage	From 2 m above the surface level, to a soil depth of 289 cm.
Vertical resolution	4 levels of the ECMWF surface model: Layer 1: 0 -7cm, Layer 2: 7 -28cm, Layer 3: 28-100cm, Layer 4: 100-289cm. *Some parameters are defined at 2 m over the surface*
Temporal coverage	January 1950 to present.
Temporal resolution	Hourly
File format	GRIB
Update frequency	Monthly with a delay of about three months relatively to actual date.

The ERA5 temperature data was downloaded for the whole Yamal peninsula and shows evidence of the temperature gradient for the north and south extend. The average temperature in January is below minus 20 °C, and more then 10 °C in July as shown in Figure 3.3.

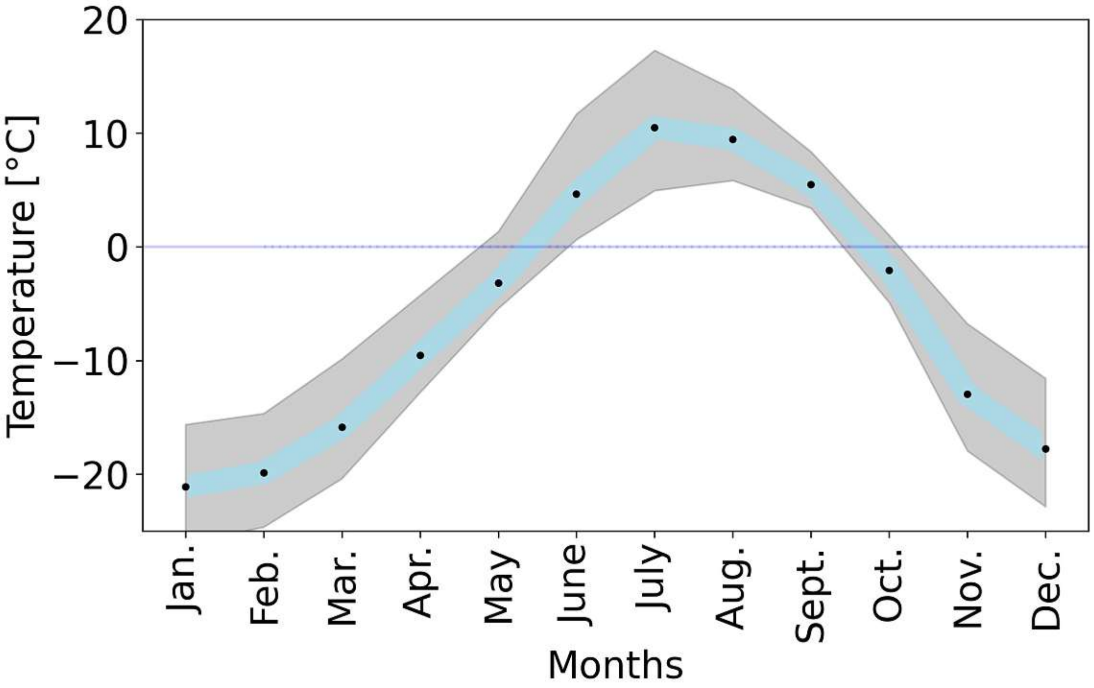

FIGURE 3.3: ERA5 temperature data for the Yamal peninsula. The covered data period is from 2015 to 2021. The horizontal blue line shows the 0 °C boarder. The mean values covering the whole Yamal peninsula are represented as black dots, the blue line connects the black dots from each month and the grey area shows the mean max and the mean from the min values for each month.

3.2.4 Field observations

Field observation data was available for four different sampling points. The data included sites close to the Erkuta river and for the Obskaya station on the 2nd of August in 2016. Those are not included in the study because of the location of a nearby river (seasonality problems at the Erkuta river site) and the other two sites for the Obskaya station were excluded because they are situated to far in the south. The used data was collected on the 26.07.2016 from the first site in the area of the Erkuta river but is not influenced by it. The location of the presented data in 5.4 is shown in the Figure 3.1 indicated as green triangle with the letter 2 on top. The featured lake had water level fluctuations at least since 1984. The analyzed basin in our data was formed during a drainage event around 2010. The conducted parameters (in %) for the sampling points in the field were: Bare soil, Sand, Clay, Litter, Moss, *Carex*, *Eriophorum*, *Poaceae*, Forbs, *Salix*, Shrubs, *Equisetum* and Vegetation coverage in total. Additionally field data parameters: coordinates, comments and the distance from the starting point (meters).

The Figure 3.4 shows an image of a typical sample location from the field survey.

FIGURE 3.4: Example of a sample plot from the field data, clearly visible is the measuring tape. Image taken on Tuesday, 26^{th} of July in 2016, at 17:27 by Dorothee Ehrich.

Chapter 4

Methods

At first the Landsat trend product was used for identification of potentially drained lakes. Objects were then manually selected representing a north – south gradient of the peninsula. The basin age was identified using the original Landsat records (4.1) based on the change of the covered water area during the years. For events after 2015 (basin ages younger then 2015) cloud free Sentinel-2 images have been used for the recent years (till 2022) to identify the drainage event and the corresponding basin age. Different remote sensing indices have been calculated for the DLBs from Sentinel-2 data (4.4). A landcover classification was used to generate annual landcover units (4.5) and buffer areas were calculated (4.3). For the analysis the average fraction for each unit within the selected basins was calculated per each year as described in Section 4.6. In the end a comparison with the landcover derived parameters and available *in situ* data was carried out (4.7).

4.1 Lake selection and age determination

A first selection of potential DLB objects was carried out using the "Hot Spot Product" Nitze et al. (2018) (Data described in 3.2.2). Lakes were highlighted according to their given attributes, for example: Net lake area change in percent (nt_ch_pc). Different possible DLBs development stages were selected and the main focus was set on the lake position to cover all present bioclimate subzones on the Yamal peninsula.

A second filtering was done to exclude false detected DLBs caused by e.g. flood plain related water area change. Lakes were also excluded when no drainage event could be detected, this could happen due to refilling, unclear drainage or when the lake drained before 1984. The detection of the drainage event and the cleaning of the false detected

DLBs was done *via* visual inspection of past imagery Landsat data. Therefore the Google Earth Pro Historical Landsat Timelapse Imagery was used for each selected object on a timeline since 1984. For Lakes which drained between 2015 and 2022, a different method was used. The landcover unit #1 (water) was investigated. Areas were highlighted that were not classified in unit #1 for the following year. Inspection of the Sentinel-2 imagery data was done and the basin excluded if necessary. The trend dataset provided the corresponding lake extend Nitze (2018) and the DLB was merged into our database. The corresponding age of the selected DLBs were then calculated for each used Sentinel−2 acquisition. The DLBs age is the difference of the year of the used satellite data and the year when the drainage event took place.

Only DLBs with a maximum water extent (status before drainage) of larger than 1 ha were eventually considered. A buffer area of 1 km extent has been derived based on the maximum water extent and is referred to a peripheral area in the following.

4.2 Pre-processing steps

The processing for Sentinel-1 is shown in the Figure 4.1 and the processing steps for Sentinel-2 on an individual image is shown in the Figure 4.2. Those steps are done within an anaconda environment for the programming language python v3 and within the Science Toolbox Exploitation Platform: SNAP.

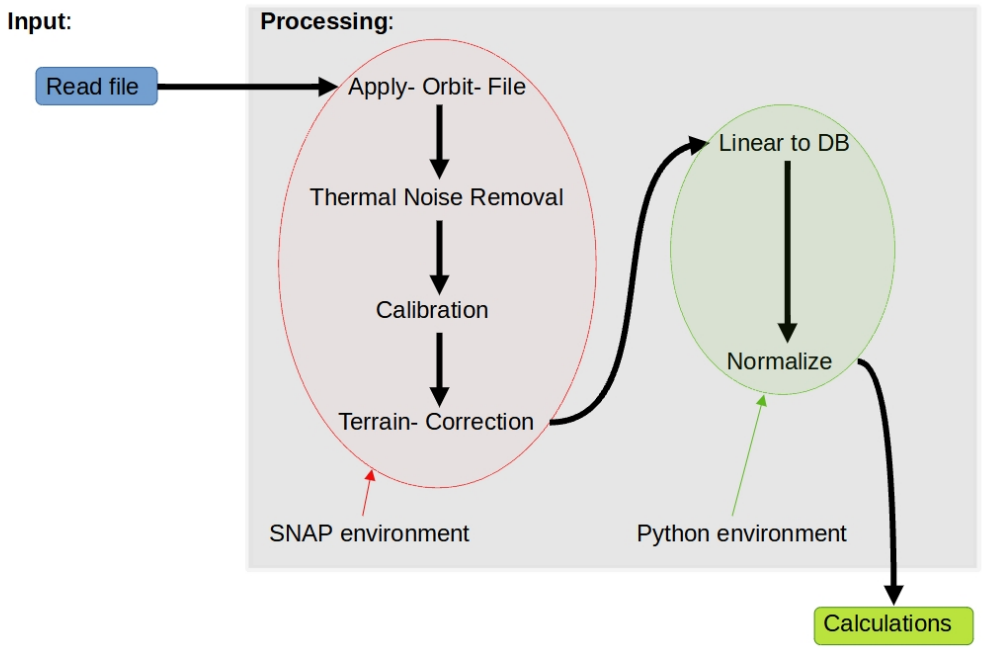

FIGURE 4.1: Processing steps of a Sentinel-1 product. The downloaded data is the input file, and undergoes different processing steps. The red cycle indicates processing done in the SNAP environment and in green the processing in python.

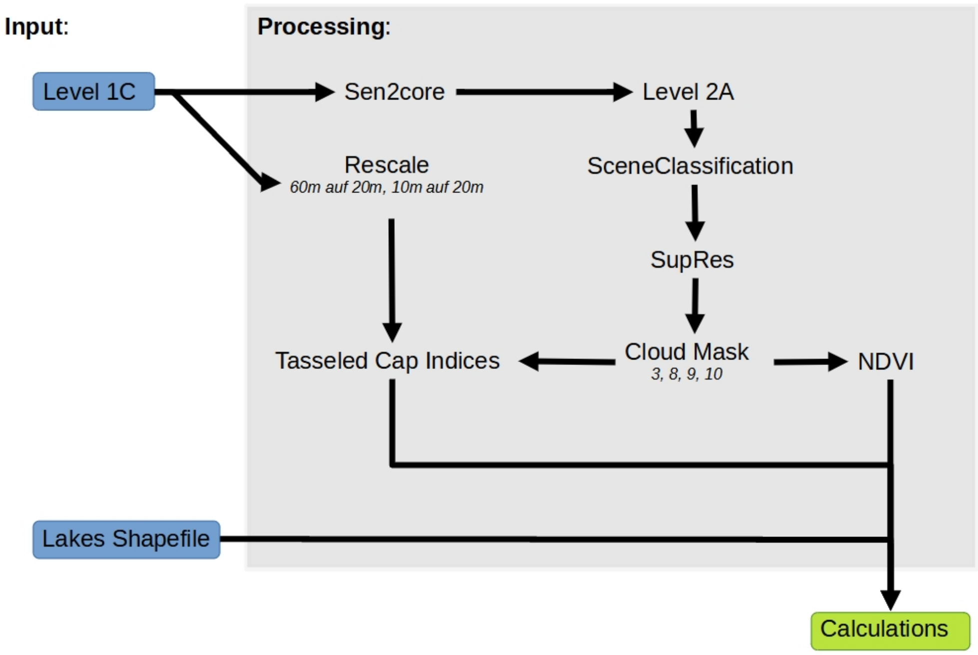

FIGURE 4.2: Workflow for a Sentinel-2 product. The downloaded data is processed in different ways, depending on the needed output. For the TCI the processing included a re-scale before calculation only but for the NDVI the Sentinel-2 data was calculated from TOA to BOA using the Sen2core.

4.3 Retrieval of the reference areas

The reference areas were retrieved for the selected lakes from the Nitze (2018) trend change dataset for a certain buffer zone (1 km) around the lake polygon. The area within the specified distance was defined as the buffer area. The buffer was calculated as vector polygon from the original input polygon. This step was done using the QGIS v3.28 software using the QGIS buffer tool.

4.4 Retrieval of indices

Different landcover metrics such as NDVI and TC indices were calculated from Sentinel−2 Products as introduced in Section 2.3.2 and 2.3.2. The calculation for the TC was done on the Level−1C Product on TOA for each pixel within the selected DLB areas. The Tasseled Cap coefficients were adjusted to the corresponding satellite according to (Crist, 1985). The spectral TC indicators were then calculated for brightness, greenness and wetness. The NDVI was calculated on BOA using the Sen2Core processor toolbox from

ESA as described in 4.5. The change in NDVI values can be associated with the loss of water area (negativ NDVI values) and colonization of the vegetation (positiv NDVI values) in the basin. The yearly NDVI data is masked for open water bodies using the corresponding landcover product for each year during the investigated time period (2015 - 2022).

4.5 Retrieval of landcover

The landcover units were retrieved following the approach developed by Bartsch et al. (2019b) and had been adapted considering advanced pre-processing (similar as in (Bartsch et al., 2021)) for each pixel within the selected DLB areas. This developed pathway focuses on the Arctic Tundra Biome and was developed within the ESA DUE Globpermafrost and `Permafrost_cci` projects. The derived landcover units are assigned to specific moisture gradients and vegetation compositions. This landcover product was generated for each year for each lake on each pixel.

The Sentinel-1 input data was downloaded from the Copernicus open access hub in VV polarisation and in Interferometric Wide (IW) swath mode. The effect of temperature on the backscatter data (Bartsch et al., 2023b, Bergstedt et al., 2018) was minimized by using acquisitions only within a certain ground temperature range. The ground temperature data was calculated from reanalyses data (ERA5). The defined temperature window reached from -10 to 0 °C.

Five spectral bands were used from the Sentinel-2 satellite data. The bands 3 (green, 10m), 4 (red, 10m), 8 (NIR, 10m), 11 (SWIR, 20m) and 12 (SWIR), 20m. Acquisitions between July and August were used to cover mid-growing season from vegetation only.

Sentinel-1 processing steps were done *via* the SNAP toolbox provided by the European Space Agency and γ^0. This included; border noise removal which was done following the bidirectional all-samples method (Ali et al., 2018), calibration, thermal noise removal and orthorectification using a DEM digital elevation model (Copernicus DEM at 90m resolution).

The data was then masked for a spatial extent of 100 x 100 km to cover the corresponding Sentinel-2 granules. The Sentinel-1 data acquired during frozen conditions represents surface roughness in tundra regions and complements the information contained in the Sentinel-2 bands.

The Sentinel-2 data was downloaded as TOA, Level-1C product and processed to BOA, Level-2A product. Therefore atmospheric-, terrain- and cirrus corrections were performed using the Sen2Core processor toolbox from ESA. For this thesis the data was then processed with super-resolution (Dsen2) for the Sentinel-2 Bands to utilize their multi-spectral capabilities due to the different spatial resolution. The tool Dsen2 (Lanaras et al., 2018) outperforms simpler upsampling methods because it preserves spectral characteristics (Bartsch et al., 2023a). Main difference to other upscaling methods is that a convolutional neural network is used. Clouds were masked using the Scene Classification Map (SCM) from the Sen2core product on the upscaled version.

A supervised maximum likelyhood classification was performed on the processed input data. The units for the supervised classification were originally derived from a k-means unsupervised classification done by (Bartsch et al., 2019b) on a 100 km wide and 1400 km long transect in Western Siberia (along the 70° meridian, from 61° North to 74° North).

In a final step the separation into the different landcover units from the CALU product was modified as shown in Table 4.1. The unit #1 was merged with the CALU units #22 'snow/ice' and #23 'other, shadow' into one 'water' unit #1. Shadow is often generated over lakes due to lower values in the spectral band. The original CALU approach uses tree different input images from Sentinel-2 for robustness of the retrieval (e.g. handling potential haze, failure of cloud masking). For the more temporally detailed approach in this study, only one input image from Sentinel−2 was used. The naming and coloring for the landcover units followed Bartsch et al. (2023a). This includes grouping recommendations which have been followed for the comparison to NDVI:

- **Group A:** 7 different units focusing on vegetation assessment. This group can be used for comparison with the CAVM.
- **Group B:** 4 different units according to their wet − dry conditions. The forest units and the unit #1 ('Water' were also included in addition to the original grouping. The unit #17 'Recently burned or flooded, partially barren' were left out.

The groups wet and moist (variant B) have been assessed with *in situ* data to justify the differentiation.

TABLE 4.1: Legend for the landcover units based on (Bartsch et al., 2023a).

ID	Description	Group A	Group B
1	water	water	water
2	shallow water / abundant macrophytes	wetland	wet
3	wetland, permanent	wetland	wet
4	wetland, seasonally inundated	wetland	wet
5	moist tundra, abundant moss, prostrate shrubs	grassland	moist
6	dry to moist tundra, partially barren, prostrate shrubs	lichen and moss	dry
7	dry tundra, abundant lichen, prostrate shrubs	lichen and moss	dry
8	dry to aquatic tundra, dwarf shrubs	shrub tundra	moist
9	dry to moist tundra, prostrate to low shrubs	shrub tundra	moist
10	moist tundra, abundant moss, prostrate to low shrubs	shrub tundra	moist
11	moist tundra, abundant moss, dwarf and low shrubs	shrub tundra	moist
12	dry to moist tundra, dense dwarf and low shrubs	shrub tundra	moist
13	moist tundra, dense dwarf and low shrubs	shrub tundra	moist
14	moist tundra, low shrubs	shrub tundra	moist
15	dry to moist tundra, partially barren	shrub tundra	moist
16	moist tundra, abundant forbs, dwarf to tall shrubs	shrub tundra	moist
17	recently burned or flooded, partially barren	shrub tundra	
18	forest (mixed)	forest	moist
19	partially barren	barren	dry

4.6 Post-processing of landcover

The landcover was post-processed and the fraction was derived for each CAL Unit within each basin. The polygon from the Nitze (2018) dataset was used to crop the data and only the inside of the basins were analyzed. The fraction was derived *via* the Formula:

$$\frac{n_{unit}}{n_{basin}} * 100 \tag{4.1}$$

where n_{basin} is the number of pixels inside the basin and n_{unit} is the number of pixels classified as a certain unit (for example #1 'water') inside the basin.

4.7 Wetness gradients evaluation with *in situ* observations

The Group B, wetness gradients derived from the landcover classification was evaluated with the field observations. In the field, plots were made on a straight line (see Figure 4.3). This *in situ* transect started at the edge of the DLB and headed to the open water body. The starting point for the first plot is at N68.18077° E69.05803°, and the last plot at: N68.17712° E69.05982°. In between eight sample plots were set.

The center points of each sample plot were taken and the corresponding landcover was generated. The individual units were grouped into the wetness gradients (see Table 4.1). The "vegetation cover total" parameter from the field data was used as the 100 percent in the calculation for the vegetation coverage. The coverage parameters on Sand and Litter were not included because the focus was set on vegetation for this thesis. The derived wetness gradients from the landcover were then used to differentiate the coverage of the vegetation communities from the field (see Figure 5.7).

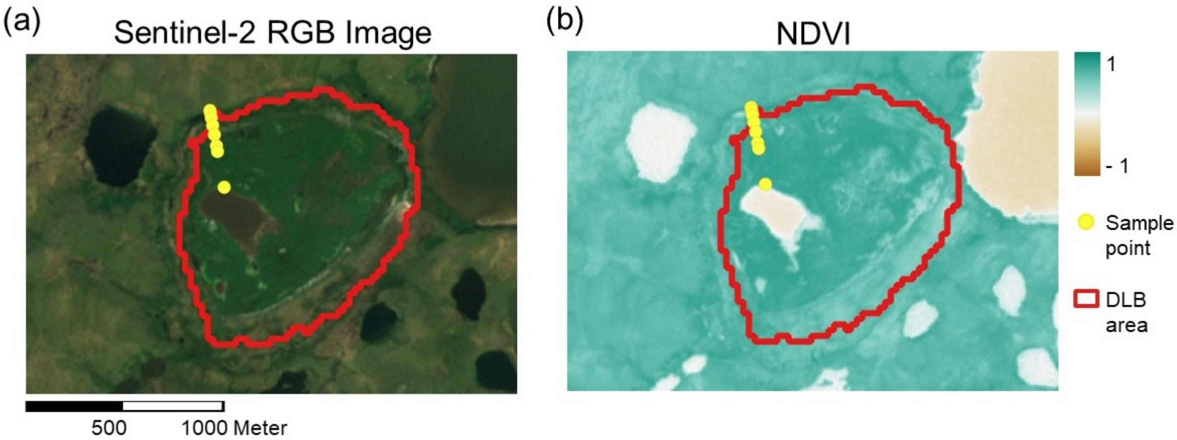

FIGURE 4.3: (a) RGB Sentinel-2 image six days before the *in situ* data was collected. (b) shows corresponding NDVI values for the 20.07.2016. over the study area.

Chapter 5

Results

137 Sentinel-2 scenes were evaluated. In the entire study area, 30 consecutive ages of DLBs were investigated. The covered ages reached from -5 to 24 years when year 0 was the year of the event of the drainage. The time-frame for DLBs events started in 1998 and ended in 2021. Most of the events were detected in 2019 with 15 different drainage events but for many years no DLB event could be detected. A total of 51 different recent DLBs were achieved. The 'water' areas of the former lakes ranged between 0,24 and 6,87 km^2. The data was limited to a basin age of 20 years as shown in the Figure, 5.2, 5.4 and Figure 5.3.

5.1 NDVI change of DLBs

The NDVI change over time for the DLBs is shown in the boxplot 5.1. The lower quantile and the higher quantile cover a wider range for the basins for all ages compared to the peripheral area where the quantiles are closer at the median. For the year 0 (the year of the drainage) the median NDVI values between the area around the basin (peripheral area) and the basin differ for more then 0.3 units. Six years after the drainage the values overlap. For the next nine years it is not possible to distinguish between the NDVI values for the peripheral area and the values inside the basin for the median values. For the DLBs ages 16 - 20 only few data is available and only the median values are shown in the boxplot. The NDVI for the peripheral area is stable over the years at around 0.5 units. Some year to year differences could occur as for the DLBs age 6 and only the median values were given.

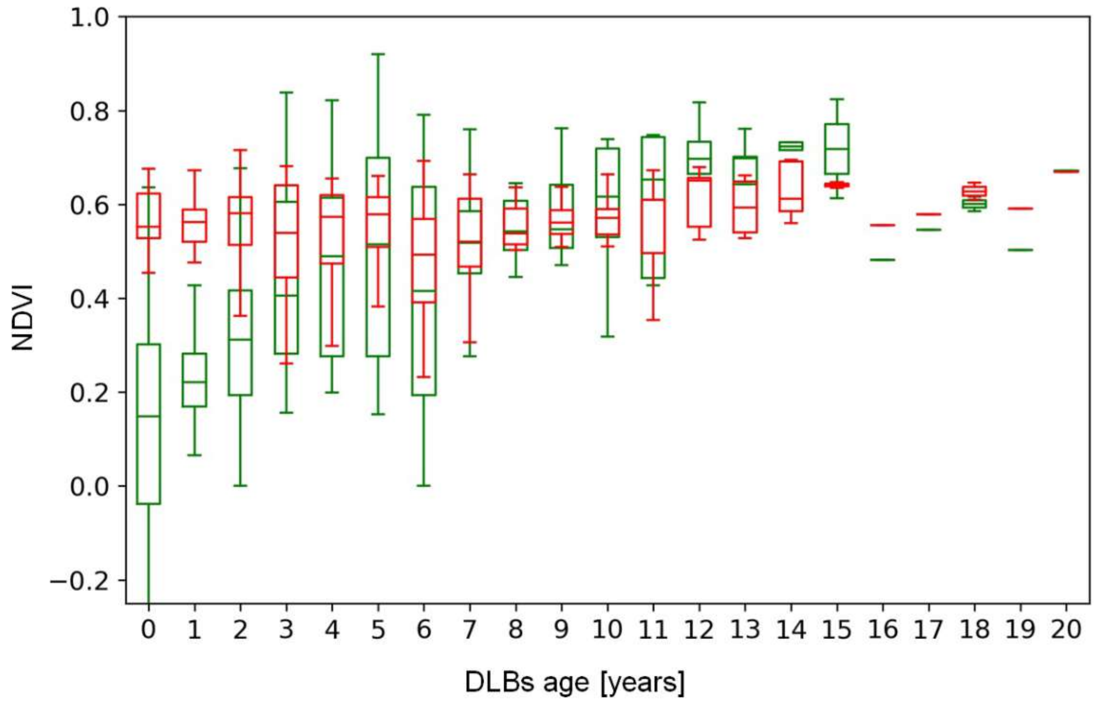

FIGURE 5.1: NDVI change over time for DLBs. After six years the peripheral and the basin NDVI values overlap sustainable. The water is masked with the generated landcover for open water bodies. Peripheral area is the area around the DLBs for a zone of 1 km. Less data is available for the last five ages.

5.2 Landcover succession in DLBs

In the Figure 5.2 the temporal change *per anno* of the 19 landcover units is shown. The data availability changes a lot, especially for the last 10 years the number of available basins drop below 10 and below five for the last five years. 'Water' #1 fraction changes from more then 70 percent to below 15 percent in the year of the drainage event. The 'barren' #19 fraction increases to more then 20 percent in the first year after drainage and slowly decreases over the following years. The fraction for prostrate and dwarf shrubs (landcover units #5, #6, #7 and #8) increase after the first year after the drainage and max at about 30 percent. After 5 years the fraction for low shrubs (#9, #10, #11, #12, #13 and #14) nearly reache 20 percent. The fraction of 'moist tundra, abundant forbs, dwarf to tall shrubs' (#16) continuously increase after the second year after drainage and after the 11 $_{\mathrm{th}}$ year maximises at close to 30 percent.

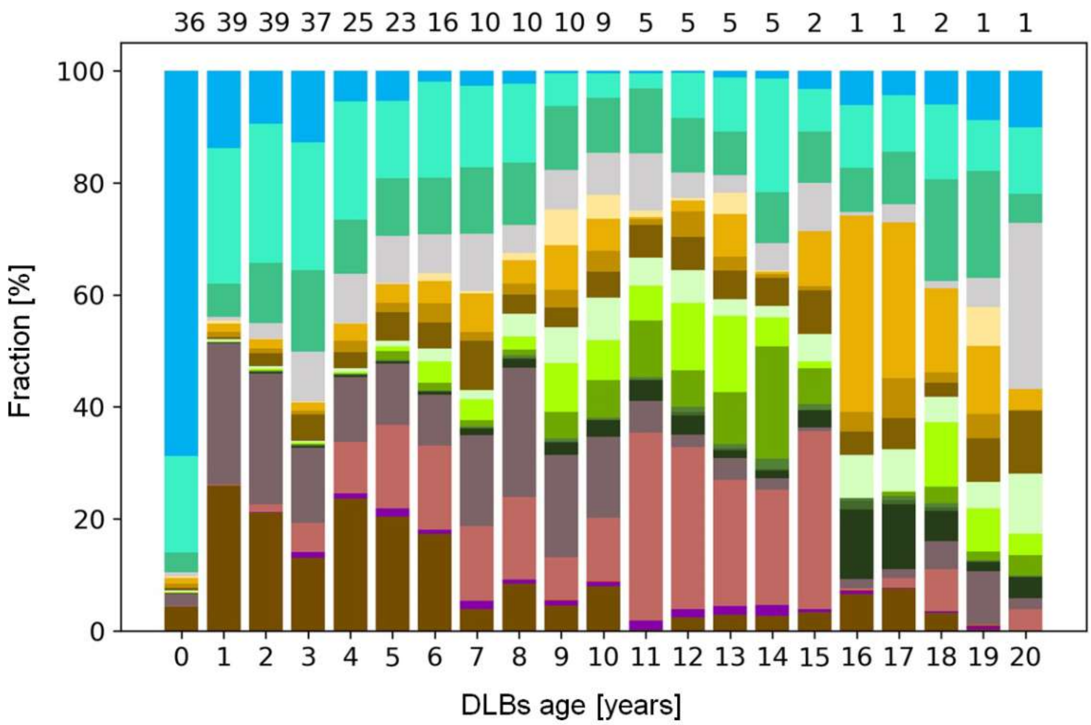

FIGURE 5.2: Annual landcover change for DLBs for the year of drainage and 20 years after. The available basin number is displayed on top of each bar. The colors are the same as shown in 4.1.

5.2.1 Group A, vegetation change of DLBs

The landcover units are grouped by their vegetation characteristics as introduced in 4.1. The yearly change for the selected DLBs is shown in Figure 5.3. The 'wetland' fraction is around 25 percent after the drainage event and nearly stayed the same during the 20 years. A slow decrease of the 'wetland' fraction is visible till the 10^{th} year, in contrast the fraction of the 'shrub tundra' group which increased during the years and even colonized more then 50 percent of the basin. The 'barren' group change over the year is the same as in Section 5.2.2. The 'grassland' and the 'forest' fraction stayed below 5 percent but an increasing trend in the 'grassland' fraction after the sixth year after drainage is visible. The fraction of the 'lichen and moss' group slowly increased during the years but stayed below 20 percent.

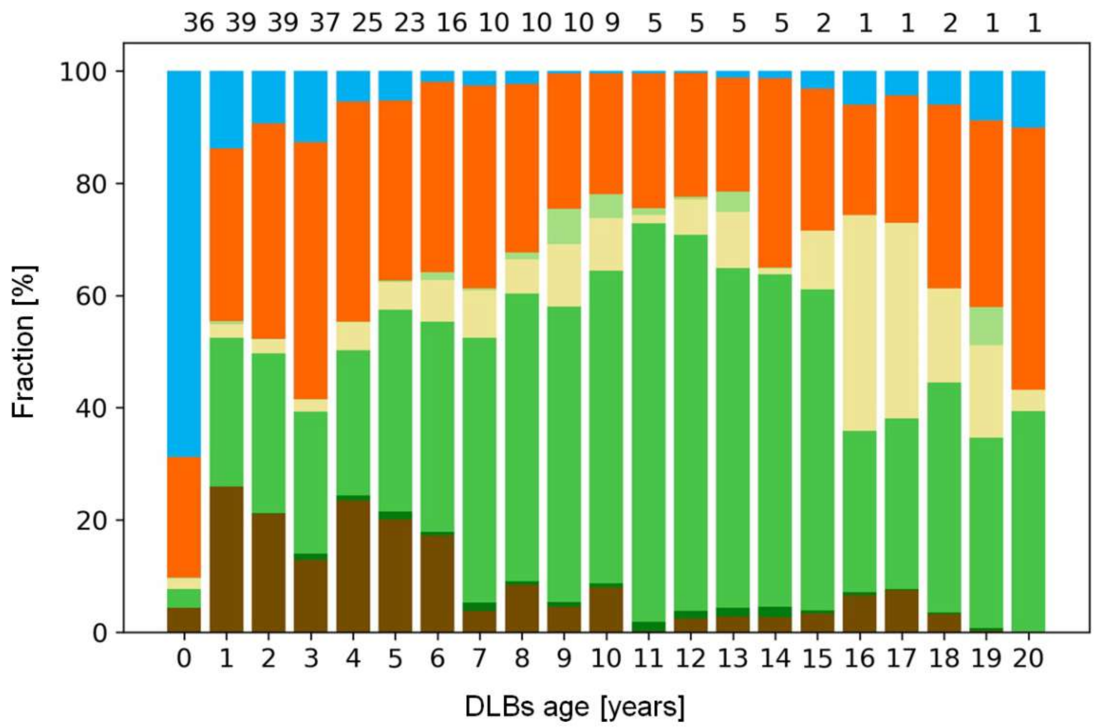

FIGURE 5.3: Fraction change of the vegetation groups (see Table 4.1) for different DLB ages (0 - 20). The number of available basins is displayed on top of each bar. The colors are the same as shown in Table 4.1.

5.2.2 Group B, wetness gradient change of DLBs

The landcover units are grouped by their wetness gradients as introduced in Table 4.1. The yearly change for the selected DLBs is shown in Figure 5.4. The fraction of the 'wet' group is around 25 percent after the drainage event and remained almost the same over the course of 20 years. A slow decrease of the 'wet' fraction is visible in the data till the 10^{th} year. *Per contra*, the proportion of the 'moist' group increases over the years and even reaches more than 50 percent in the basin. The 'Dry' fraction increases to more then 20 percent in the first year after drainage and slowly decreases over the following years. In the 16^{th} and 17^{th} year the 'Dry' fraction reaches around 40 percent but the number of available basins drops to 1 available basin for the analysis.

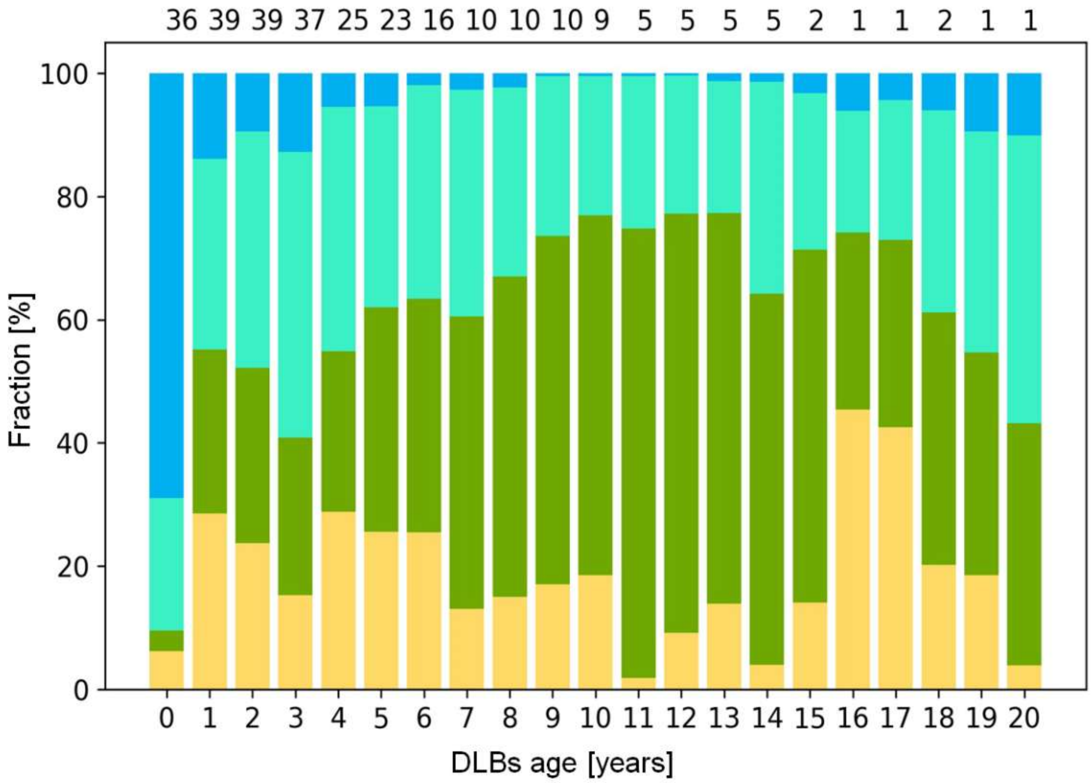

FIGURE 5.4: Wetness change for the DLBs for the year of drainage and 20 years after. The number of available basins is displayed on top of each bar. The colors are identical with the CALU (see Table 4.1).

5.3 Case study

One recently DLB is investigated on the change of the Indices (Section: 5.3.1) and the corresponding change in the landcover (Section: 5.3.2) is shown in detail.

5.3.1 Change of indices for a selected DLB

The years 2016, 2017, 2018, 2019, 2020 and 2020 show an increase in the indices for NDVI, TC brightness and TC greenness as shown in Figure 5.5. The index for TC wetness shows a different trajectory. For the years 2016, 2017 and 2018 a decrease in the TC wetness is shown following an slow increase for 2019 and 2020. For 2021 the values show again a small decrease compared to the previous year. The satellite data shows different greening hot spot locations in the basin. In 2016 no vegetation can be seen and bare soil is shown in the basin, with one exception, some remaining water area in the northern part. In 2018 greening can be shown in the northern part of the basin. In 2021 nearly the whole area of the basin is green, and the remaining water area in the north is still visible. Also the green in the northern part is darker inside the basin than in the south.

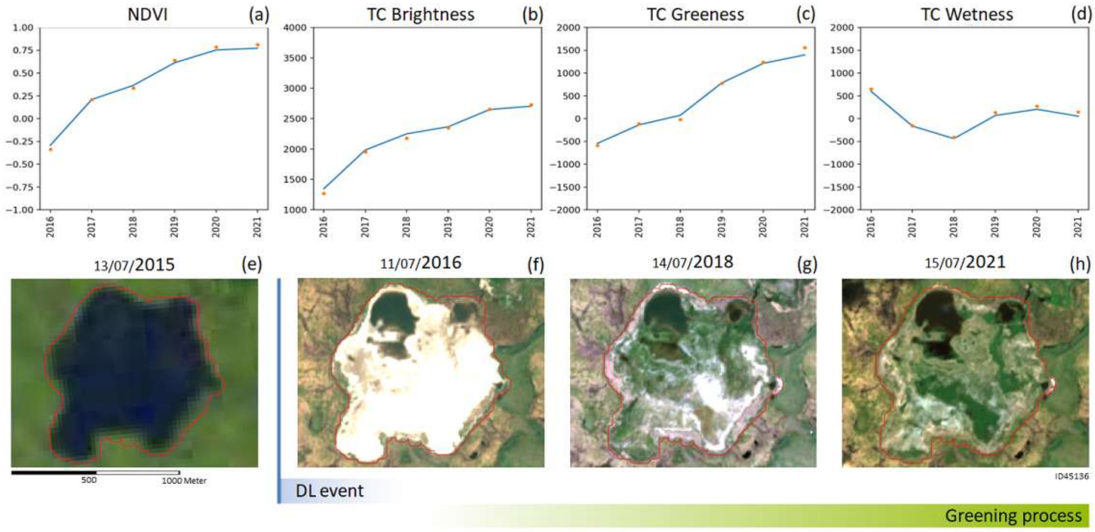

FIGURE 5.5: (a) NDVI values and (b - d) TC brightness, greenness and wetness values for the years 2016 – 2021. RGB data from (e) Landsat and from (f – h) Sentinel-2 satellite data after a drained lake event. In red the polygon lake area is shown. The polygon is derived from Nitze (2018) including a 30 meter buffer. The basin is located on the eastern part of the Yamal peninsula as shown in Figure 3.1 and is indicated as a green cycle with the number 2 on top of it.

5.3.2 Change of landcover for a selected DLB

Annual generated landcover for an example lake is shown in (Figure 5.6. The example lake is located on the eastern part of the Yamal peninsula as shown in Figure 3.1 and is indicated as a green cycle with the number 2 on top of it. The drained lake event occurred between 2015 (visual inspection showed full water area) and 2016. Whereas in the summer 2016 the Sentinel-2 image shows that the lake is already drained. Small 'wetlands' form during the years after drainage especially in the northern part of the basin and water (#1) areas remain. The 'barren' units #19 and #15 are present with a high fraction for the first two years (2016, 2017) after the drainage event. In the year 2021 the fraction for #16, 'moist tundra, abundant forbs, dwarf to tall shrubs' starts to increase in the DLB. Water areas (#1) in the north of the basin are still visible six years after drainage.

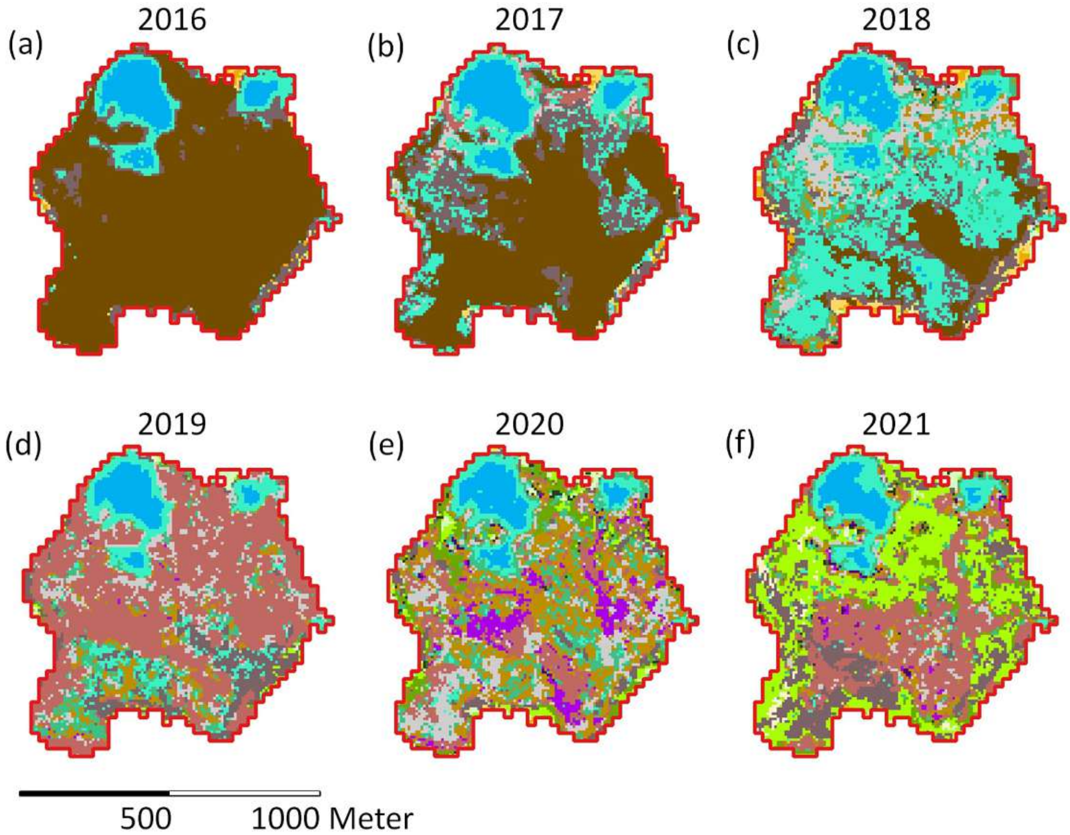

FIGURE 5.6: Annual generated landcover for a recently drained lake as shown in Figure 5.5, (a - f) presents the years from 2016 to 2021, for landcover legend see Table 4.1.

5.4 Comparison of wetness groups to field data

The field data shows that the soil of the basin is clay. Some litter was found inside the eight sample areas. Vegetation cover was 80 percent or above at the date of the fieldwork. The collected field data is shown in Table 5.1 at the 26_{th} July in 2016. Distance from the first Plot: 14, 39, 80, 130, 190, 220 and 413 meters. The wetness gradients 'moist' and 'wet' are used to differentiate vegetation communities (see Figue 5.7) based on their presence but no data is available for 'Dry'. Five sample plots are classified for the 'moist' and three sample plots are classified in the 'wet' CALU group.

TABLE 5.1: FIELD INVENTORY OF LAKES IN YAMAL 2016, conducted by Dorothee Ehrich.

	Plot 1	**Plot 2**	**Plot 3**	**Plot 4**	**Plot 5**	**Plot 6**	**Plot 7**	**Plot 8**
Distance from 0 [m]		14	39	80	130	190	220	413
Bare soil cover [%]	0	0	0	0	0	0	2	5
Sand	0	0	0	0	0	0	0	0
Clay	0	0	0	0	0	0	2	5
Moss cover [%]	3	10	15	1	1	0	3	5
Carex [%]	77	1	50	30	1	0	0	0
Eriophorum [%]	0	0	0	50	85	0	0	0
Poaceae [%]	0	1	3	5	7	95	30	95
Forbs [%]	3	<1	3	0	<1	0	55	0
Salix [%]	0	0	0	0	0	0	0	0
Shrubs [%]	0	0	0	0	0	0	0	0
Equisetum [%]	0	80	20	0	0	0	0	0
Vegetation cover total [%]	80	90	90	85	95	95	98	95
Litter [%]	20	10	0	15	5	5	0	0

Addition: - between Plot 4 and Plot 5 some Salix shrubs (about 7 shrubs), h *ca.* 50 cm
- Plot 5: soil under vegetation = sand
- between Plot 6 and Plot 8 vegetation like on Plot 6 with *Eriophorum scheuchzeri* patches and *Carex* stans patches.

The sample plots assigned to the ‘wet’ group are mostly dominated by *Equisetum* and *Poaceae* plants as shown in Figure 5.7. One *in situ* sample plot contained more then 80% coverage of horsetail (*Equisetum*) and is classified as ‘wet’ indicating high wetness. *Poaceae* is present in more then one sample plots. The ‘moist’ group shows more heterogeneity in the vegetation data. The coverage of *Carex* and *Poaceae* reach from 0% to over 90%, covering a wide window on wetness information reaching from ‘moist’ to ‘wet’ as shown in Figure 5.7.

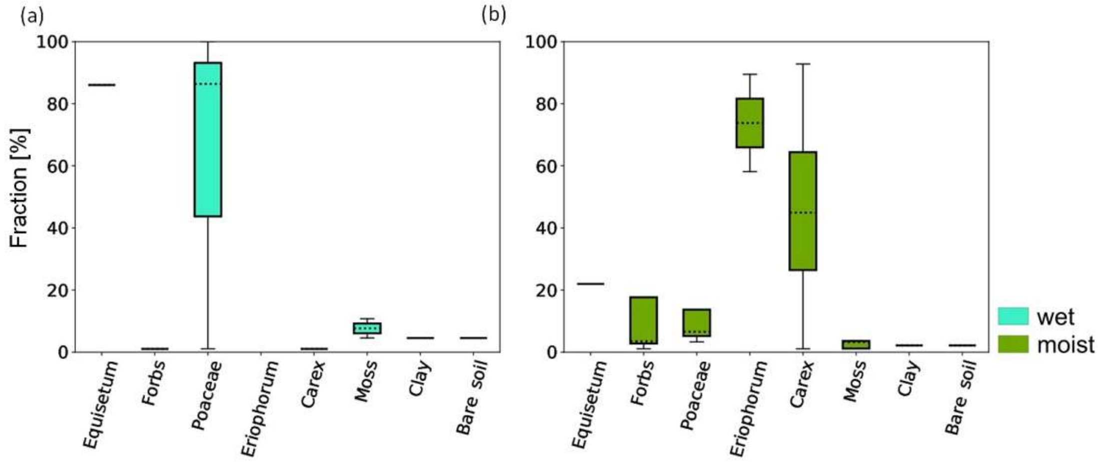

FIGURE 5.7: Types of surface data conducted in the field, separated for the corresponding classified pixel (a: moist, b: wet). Eight different surface categories are distinguished, vegetation related (*Equisetum*, Forbs, *Poaceae*, *Eriophorum*, *Carex*, Moss) and soil related (Clay and Bare soil). Field data conducted by Dorothee Ehrich, for the location of the drained basin see Figure 3.1, indicated as green cycle with the number 1 on top of it.

Chapter 6

Discussion

The thesis showed that the open water fraction is decreasing during time for the basin which might implicate changes in the Permafrost (Göckede et al., 2019, Swanson, 2022). There are also seasonally patterns which appeared to repeat annually and should be addressed. In Figure 6.1 greenness fluctuations and wet areas are clearly visible in the center of the basin as the satellite images showed at the beginning and end of July (for 2018 and 2019). Also the water depth might play a role on seasonal dynamics (Dai et al., 2019). The vegetation showed a seasonally inundated landcover and included waterlogged dynamics. This might be assisted by sparse and fast growing vegetation, likely Graminoids (Magnússon et al., 2020). The repeating dynamics can be seen in the NDVI for end of July. Depressions in the topology might be the cause for the more wet areas which can be seen in the TC composite image as blue.

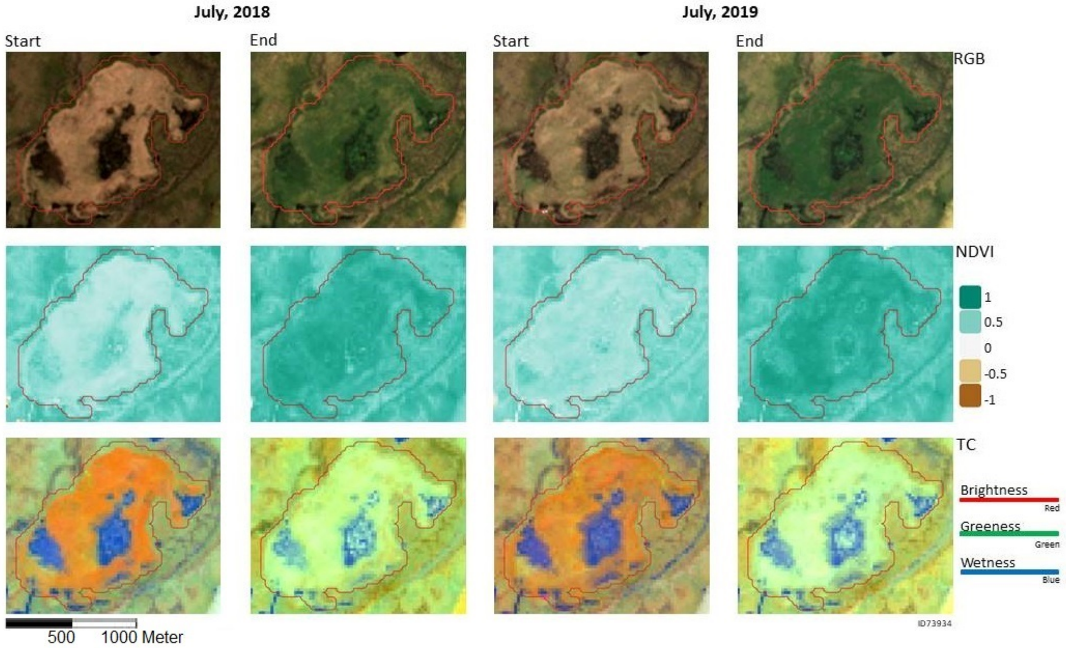

FIGURE 6.1: Inter-annual dynamics for a selected DLB in Yamal. The basin is located in the center - east part of the peninsula indicated as a green cycle with the number 3 on top of it (Figure 3.1). The red polygon line indicates the boarder of the former lake area Nitze (2018). The first row shows the RGB images, the second the NDVI and the last row shows the TC composite image. The NDVI shows values greater then 0 indicating the presence of vegetation. The TC composite image indicates red for TC brightness values, green for TC greenness and blue for TC wetness values.

Lakes and their hydrological connection can influence each other Liu et al. (2023a) and also their connection in drainage mechanisms should be discussed. The RGB images in Figure 6.2 show two basins with water level exchange from 2015, 2016, 2017 and 2019. In 2016 the lake located on the west side fully drained compared to the lake located at the east side which only drained partly. This might be *via* a Channel, like a depression in the topography. Also another lake located in the south east corner had lower water level in 2016 but refilled in 2017. The lake on the east side refilled with water in 2017. The started greening process is visible for the west basin. In 2019 the west basin is green and the water area returned at the east lake partly which might indicate hydrological connectivity.

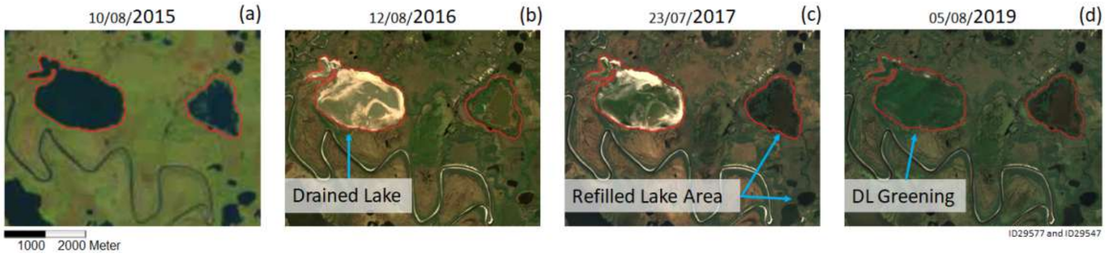

FIGURE 6.2: Hydrological connectivity for different lakes. RGB data in (a) Landsat and (b – d) Sentinel-2. The DLB greening process is shown between 2015 and 2019 for the basin located in the west of the image. Water refilling occurred at the basin on the east. The polygon line is derived from Nitze (2018). The lakes are located at the center-west of Yamal (see Figure 3.1, indicated as green cycles with the number 4 on top of it).

The drainage mechanism can happen *via* a lateral thermokarst lake drainage event (see Figure 6.3). In 2016 the water area of the future basin seemed to be intact. The river showed no sediments in the water. The lake drained in 2017 formed a drainage channel most likely due to the melting of ground ice (Chen et al., 2023). Across a distance for about 500 meters the water of the drained lake flowed into the nearby river. Sediments from the lake and the lake water were flushed into the river. The river changed color when the water passed the drainage channel which might indicate water and sediment movements from the basin. In 2018 a second drainage event happened. The lake located to the north of the former drained lake also drained. Water areas in the older basin were visible. The water in the river still changed color after entry of in the drainage channel. In 2019 the both DLBs started to green and the water area in the older basin increased a little bit. The sediments in the river after the drainage channel were still visible. The greening increased in 2020 and the refilled water level in the older basin dropped. The drainage channel increased in width which might have indicated ongoing degradation and destabilizing of the ground. Six years after the disturbance the drainage channel seemed to have no big influence on the river any longer. The area of the greening of the two basins is still increasing and no remaining water level changes are visible. The former drainage channel started to green but there is no image for 2021 (due to clouds) and therefore the greening of the drainage channel might have happened already in 2021 and not 2022.

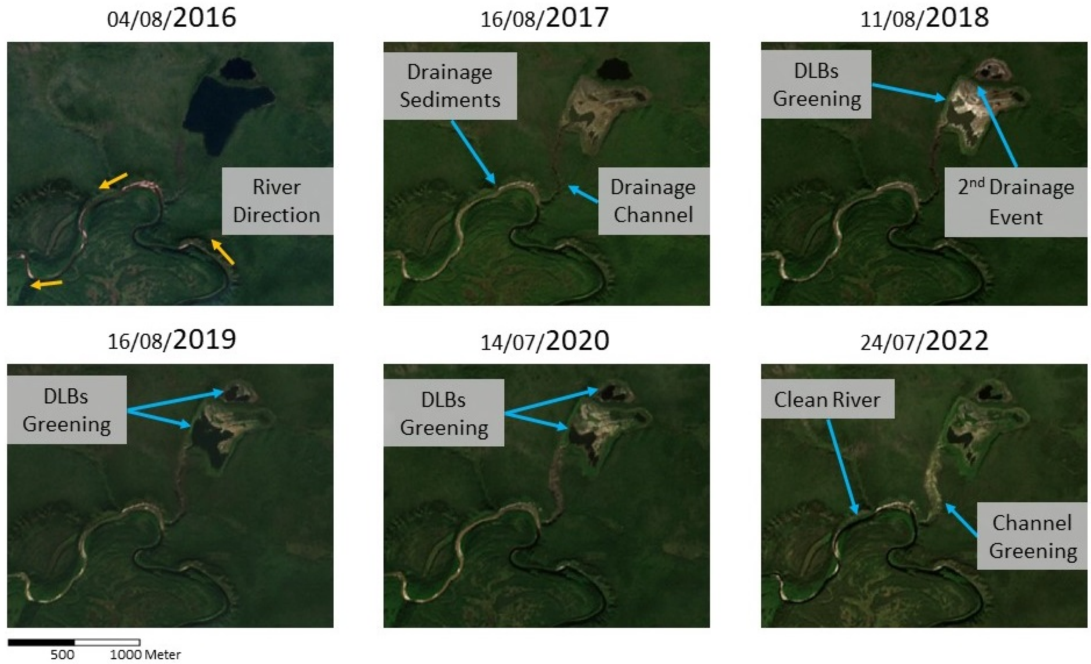

FIGURE 6.3: Process of a lateral thermokarst lake drainage event *via* a drainage channel. No cloud free data was available for the summer 2021.

Compared to remote sensing indices like the NDVI and TC only, using the annual generated landcover product additional information on succession stages and landscape changes are derived. One disadvantage is, that many data processing steps need to be included to derive the high spatial and thematic detail for the landcover. This is a complex undertaking and consumes a lot of time. Computing technology and deep learning methods help to automate large-scale assessment of land-use (Masolele et al., 2021).

The method used to create the landcover product in this work is slightly different from the original. Bartsch et al. (2023a) used the gamma angle for their Sentinel-1 processing for their landcover product, but for this thesis sigma was used. In mountainous areas the classification results might show differences, for consistency only one method should be used. A comparison for the Yamal study area revealed no big difference in the classification as shown in Figure 6.4. This is mainly due to the more or less flat terrain on the peninsula.

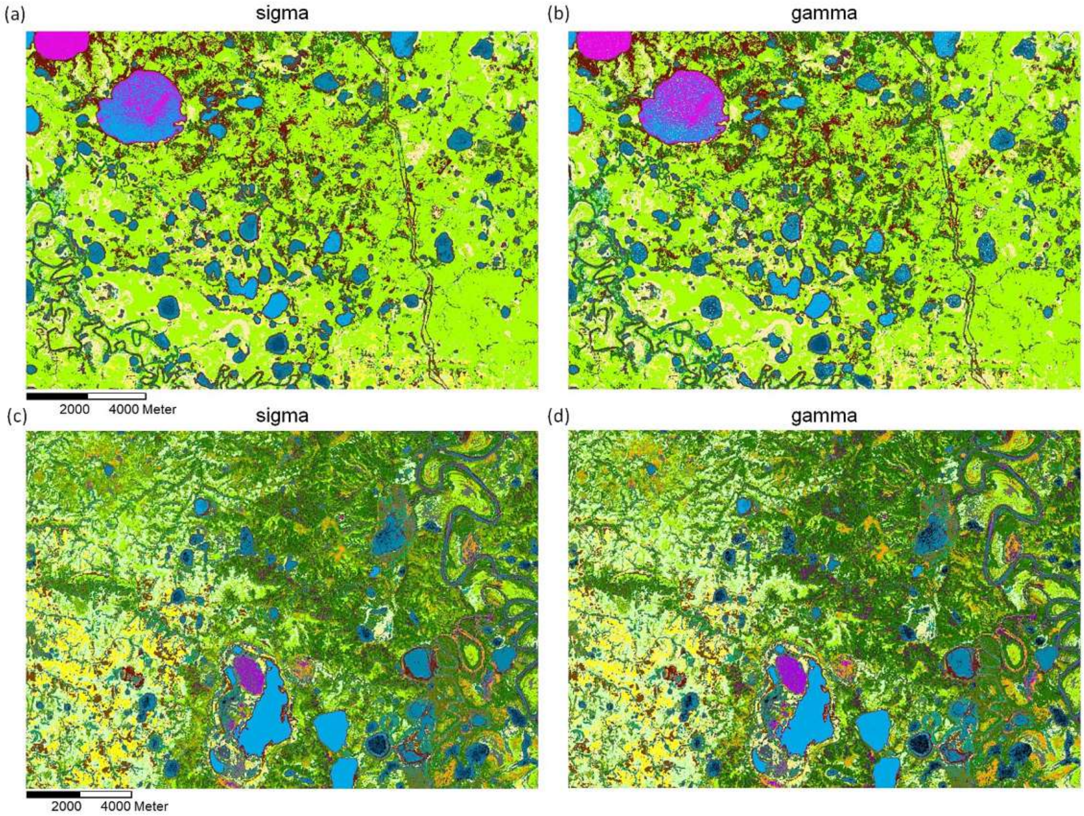

FIGURE 6.4: (a, c) generated landcover with Sentinel-1 processing for sigma, (b - d) for processing using gamma. See Table 4.1 for color legend. Landcover (a, b) for 2016 and (c, d) for 2020.

Lantz et al. (2022) found out that DLBs are typical sites of wetland formation. In the presented Figure 5.6 an DLB example was shown that developed small wetlands inside the basins after the drainage. Loiko et al. (2020) concluded that soils might be covered with a thick moss-grass layer (exceeding 10 cm) and that these wetlands are located in wet depressions. Partial drainage can cause water areas to persist within the drained basin but might vary for different basin age stages as Magnússon et al. (2020) showed.

After the drainage event the landcover has a tendency to become more heterogeneous over time as presented in Figure 5.2 and 5.6. This supports the commonly held assumption that lake drainage introduces landcover heterogeneity into the landscape (Bartsch et al., 2023b). Those changes in the landcover can be linked to Permafrost changes which need to be addressed in more detail in further research. The Figures shown in 5.2, 5.4 and 5.3 showed a high percentage of barren areas after the drainage event, this appearance of non-vegetated areas was also highlighted by Lantz (2017) in recently DLBs.

To constrain the analysis and to better be able to study the process of surface changes, basins were carefully selected, omitting those which were located in active floodplains or drained due to suspected anthropogenic influence.

To further study the complex dynamics of post drainage landcover development, basins of different characteristics should be considered. The role of climatic subzones, for example the Bioclimate subzones based on the CAVM from (Walker et al., 2005) should be addressed in further research.

Drainage events influence also the fauna. The change in landcover following a drainage event has dramatic impacts on the habitat, for example on fish populations, but on the other hand reindeer also gain new grazing ground (Kumpula et al., 2011). One also needs to think about drainage caused directly by anthropogenic activities. In August 1979 research was conducted on Richards Island in the Mackenzie delta area (Canada). Lake Illisarvik was artificially drained to investigate the change of permafrost (French, 2007). Also drainage due to oil and gas industry might influence the drainage processAdditional infrastructure data for excluding drained lakes in a certain buffer zone close to infrastructure should be looked upon in future research.

The available data changed drastic for different basin ages in the presented approach as shown in Figure 5.2. Therefore the results especially for the older aged basins should be interpreted very carefully. The landcover products for the last six years (age 15 till age 20) are only based on two and for the last two ages even only one DLB. Since the 10^{th} year after drainage the data availability dropped below 10 available basins for each year. Building age groups of DLBs which combine more years or expanding the study area would improve the number of basins and more reliable data would be acquired.

Conclusio

Improving our knowledge on processes involved in drainage events in the Arctic environment associated with permafrost conditions and surrounding terrain is crucial for numerous applications (e.g., landscape models, carbon cycle processes and local infrastructure stability).

Landcover changes in DLBs can be described with an annually generated landcover in addition to traditional SRS methods like NDVI or TC changes. The corresponding changes of biodiversity and carbon cycle need to be addressed since drainage is a common feature across the entire Arctic.

This thesis contributes to an improved understanding of the changes in DLBs, the alteration of landsurface hydrology and to a better knowledge of these unique and important landforms. It was shown that the basins of drained lakes experience landcover heterogeneity in the Arctic tundra indicating a high content of biomass and productivity from variable plant communities. It was shown that certain DLBs are influenced by site-specific factors like relative basin age and hydrological connectivity which influences the vegetation dynamics. Changes in the NDVI revealed a fast increase after a drainage event, it takes only five years till the values in the basins reach the same as the peripheral areas.

The results of the work in this thesis expand the understanding of recent DLBs and the corresponding change of flora and fauna. Wetlands in DLBs decrease slowly but can form again, after an drainage event. In contrast to this, the shrub tundra vegetation colonizes the basin in a more sustainable way. Barren areas can reoccur and new basins can be formed inside an old basin. Drainage events frequently lead to only partial drainage, causing water areas to persist within the drained basin.

DLBs can be seen as hot spots of a greening process a fact which is underlined by the results presented in this thesis. They have significant consequences for the stability of permafrost and the release of greenhouse gases. To address the relationship between permafrost - DLBs appears to be important and might be an interesting field of further research.

References

Ali, I., Cao, S., Naeimi, V., Paulik, C., Wagner, W., 2018. Methods to remove the border noise from Sentinel-1 Synthetic Aperture Radar data: Implications and importance for time-series analysis. IEEE Journal of Selected Topics in Applied Earth Observations and Remote Sensing 11, 777–786. doi:10.1109/JSTARS.2017.2787650.

Bartsch, A., Efimova, A., Widhalm, B., Muri, X., von Baeckmann, C., Bergstedt, H., Ermokhina, Hugelius, Heim, B., Leibman, M., 2023a. Arctic landcover diversity circumpolar landcover diversity of the arctic. EGUsphere [preprint] doi:10.5194/egusphere-2023-2295.

Bartsch, A., Leibman, M., Strozzi, T., Khomutov, A., Widhalm, B., Babkina, E., Mullanurov, D., Ermokhina, K., Kroisleitner, C., Bergstedt, H., 2019a. Seasonal progression of ground displacement identified with satellite radar interferometry and the impact of unusually warm conditions on permafrost at the yamal peninsula in 2016. Remote Sensing 11, 1865. doi:10.3390/rs11161865.

Bartsch, A., Pointner, G., Nitze, I., Efimova, A., Jakober, D., Ley, S., Högström, E., Grosse, G., Schweitzer, P., 2021. Expanding infrastructure and growing anthropogenic impacts along arctic coasts. Environmental Research Letters 16, 115013. doi:10.1088/1748-9326/ac3176.

Bartsch, A., Strozzi, T., Nitze, I., 2023b. Permafrost monitoring from space. Surveys in Geophysics doi:10.1007/s10712-023-09770-3.

Bartsch, A., Widhalm, B., Pointner, G., Ermokhina, K.A., Leibman, M., Heim, B., 2019b. Landcover derived from sentinel-1 and sentinel-2 satellite data (2015-2018) for subarctic and arctic environments. doi:10.1594/PANGAEA.897916.

Bauer-Marschallinger, B., Cao, S., Navacchi, C., Freeman, V., Reuß, F., Geudtner, D., Rommen, B., Vega, F.C., Snoeij, P., Attema, E., Reimer, C., Wagner, W., 2021. The normalised sentinel-1 global backscatter model, mapping earth's land surface with c-band microwaves. Scientific Data 8. doi:10.1038/s41597-021-01059-7.

Bergstedt, H., Jones, B.M., Hinkel, K., Farquharson, L., Gaglioti, B.V., Parsekian, A.D., Kanevskiy, M., Ohara, N., Breen, A.L., Rangel, R.C., Grosse, G., Nitze, I., 2021. Remote sensing-based statistical approach for defining drained lake basins in a continuous permafrost region, north slope of alaska. Remote Sensing 13, 2539. doi:10.3390/rs13132539.

Bergstedt, H., Zwieback, S., Bartsch, A., Leibman, M., 2018. Dependence of c-band backscatter on ground temperature, air temperature and snow depth in arctic permafrost regions. Remote Sensing 10, 142. doi:10.3390/rs10010142.

Brovkin, V., Brook, E., Williams, J.W., Bathiany, S., Lenton, T.M., Barton, M., DeConto, R.M., Donges, J.F., Ganopolski, A., McManus, J., Praetorius, S., de Vernal, A., Abe-Ouchi, A., Cheng, H., Claussen, M., Crucifix, M., Gallopín, G., Iglesias, V., Kaufman, D.S., Kleinen, T., Lambert, F., van der Leeuw, S., Liddy, H., Loutre, M.F., McGee, D., Rehfeld, K., Rhodes, R., Seddon, A.W.R., Trauth, M.H., Vanderveken, L., Yu, Z., 2021. Past abrupt changes, tipping points and cascading impacts in the earth system. Nature Geoscience 14, 550–558. doi:10.1038/s41561-021-00790-5.

Brown, Melnikov, Heginbottom, Ferrians, 1997. Circum-Arctic map of permafrost and ground-ice conditions. doi:10.3133/cp45.

Chen, Y., Cheng, X., Liu, A., Chen, Q., Wang, C., 2023. Tracking lake drainage events and drained lake basin vegetation dynamics across the arctic. Nature Communications 14. doi:10.1038/s41467-023-43207-0.

Chen, Y., Liu, A., Cheng, X., 2021. Vegetation grows more luxuriantly in arctic permafrost drained lake basins. Global Change Biology 27, 5865–5876. doi:10.1111/gcb.15853.

Crist, E.P., 1985. A TM tasseled cap equivalent transformation for reflectance factor data. Remote Sensing of Environment 17, 301–306. doi:10.1016/0034-4257(85)90102-6.

Dai, L., Guo, X., Zhang, F., Du, Y., Ke, X., Li, Y., Cao, G., Li, Q., Lin, L., Shu, K., Peng, C., 2019. Seasonal dynamics and controls of deep soil water infiltration in the seasonally-frozen region of the qinghai-tibet plateau. Journal of Hydrology 571, 740–748. doi:10.1016/j.jhydrol.2019.02.021.

Dobiński, W., 2020. Permafrost active layer. Earth-Science Reviews 208, 103301. doi:10.1016/j.earscirev.2020.103301.

ESA-Communications, 2011. A Document by the ESA Director Generaland the ESA Directo. European Space Agency. ISBN: 987-92-9221-004-5.

European Space Agency, 2022. Sentinel online. URL: https://sentinel.esa.int/.

van Everdingen, R.O., 1998. Multi-language Glossary of Permafrost and Related Ground-ice Terms. International Permafrost Association, University of Calgary.

Farquharson, L.M., Romanovsky, V.E., Kholodov, A., Nicolsky, D., 2022. Sub-aerial talik formation observed across the discontinuous permafrost zone of alaska. Nature Geoscience 15, 475–481. doi:10.1038/s41561-022-00952-z.

French, H.M., 2007. The Periglacial Environment. Wiley. ISBN: 9780470865897.

Gong, P., Wang, J., Yu, L., Zhao, Y., Zhao, Y., Liang, L., Niu, Z., Huang, X., Fu, H., Liu, S., Li, C., Li, X., Fu, W., Liu, C., Xu, Y., Wang, X., Cheng, Q., Hu, L., Yao, W., Zhang, H., Zhu, P., Zhao, Z., Zhang, H., Zheng, Y., Ji, L., Zhang, Y., Chen, H., Yan, A., Guo, J., Yu, L., Wang, L., Liu, X., Shi, T., Zhu, M., Chen, Y., Yang, G., Tang, P., Xu, B., Giri, C., Clinton, N., Zhu, Z., Chen, J., Chen, J., 2012. Finer resolution observation and monitoring of global land cover: first mapping results with landsat tm and etm+ data. International Journal of Remote Sensing 34, 2607–2654. doi:10.1080/01431161.2012.748992.

Göckede, M., Kwon, M.J., Kittler, F., Heimann, M., Zimov, N., Zimov, S., 2019. Negative feedback processes following drainage slow down permafrost degradation. Global Change Biology 25, 3254–3266. doi:10.1111/gcb.14744.

Hachmeister, J., Schneising, O., Buchwitz, M., Lorente, A., Borsdorff, T., Burrows, J.P., Notholt, J., Buschmann, M., 2022. On the influence of underlying elevation data on sentinel-5 precursor tropomi satellite methane retrievals over greenland. Atmospheric Measurement Techniques 15, 4063–4074. doi:10.5194/amt-15-4063-2022.

Hersbach, H., Bell, B., Berrisford, P., Hirahara, S., Horányi, A., Muñoz-Sabater, J., Nicolas, J., Peubey, C., Radu, R., Schepers, D., Simmons, A., Soci, C., Abdalla, S., Abellan, X., Balsamo, G., Bechtold, P., Biavati, G., Bidlot, J., Bonavita, M., De Chiara, G., Dahlgren, P., Dee, D., Diamantakis, M., Dragani, R., Flemming, J., Forbes, R., Fuentes, M., Geer, A., Haimberger, L., Healy, S., Hogan, R.J., Hólm, E., Janisková, M., Keeley, S., Laloyaux, P., Lopez, P., Lupu, C., Radnoti, G., de Rosnay, P., Rozum, I., Vamborg, F., Villaume, S., Thépaut, J.N., 2020. The era5 global reanalysis. Quarterly Journal of the Royal Meteorological Society 146, 1999–2049. doi:https://doi.org/10.1002/qj.3803.

Hjort, J., Karjalainen, O., Aalto, J., Westermann, S., Romanovsky, V.E., Nelson, F.E., Etzelmüller, B., Luoto, M., 2018. Degrading permafrost puts arctic infrastructure at risk by mid-century. Nature Communications 9. doi:10.1038/s41467-018-07557-4.

Hjort, J., Streletskiy, D., Doré, G., Wu, Q., Bjella, K., Luoto, M., 2022. Impacts of permafrost degradation on infrastructure. Nature Reviews Earth and Environment 3, 24–38. doi:10.1038/s43017-021-00247-8.

IPCC, 2022. Climate change 2022: Impacts, adaptation, and vulnerability. contribution of working group ii to the sixth assessment report of the intergovernmental panel on climate change. IPCC Technical Summary , 33–118doi:10.1017/9781009325844.002.

Jones, B.M., Grosse, G., Arp, C.D., Jones, M.C., Anthony, K.M.W., Romanovsky, V.E., 2011. Modern thermokarst lake dynamics in the continuous permafrost zone, northern seward peninsula, alaska. Journal of Geophysical Research 116. doi:10.1029/2011jg001666.

Jones, B.M., Grosse, G., Farquharson, L.M., Roy-Léveillée, P., Veremeeva, A., Kanevskiy, M.Z., Gaglioti, B.V., Breen, A.L., Parsekian, A.D., Ulrich, M., Hinkel, K.M., 2022. Lake and drained lake basin systems in lowland permafrost regions. Nature Reviews Earth and Environment 3, 85–98. doi:10.1038/s43017-021-00238-9.

Jones, B.M., Schaeffer Tessier, S., Tessier, T., Brubaker, M., Brook, M., Schaeffer, J., Ward Jones, M.K., Grosse, G., Nitze, I., Rettelbach, T., Zavoico, S., Clark, J.A., Tape, K.D., 2023. Integrating local environmental observations and remote sensing to better understand the life cycle of a thermokarst lake in arctic alaska. Arctic, Antarctic, and Alpine Research 55. doi:10.1080/15230430.2023.2195518.

Jones, H.G., Vaughan, R.A., 2010. Remote Sensing of Vegetation Principles, Techniques, and Applications. Oxford University Press. ISBN: 9780199207794.

Jorgenson, M.T., Romanovsky, V., Harden, J., Shur, Y., O'Donnell, J., Schuur, E.A.G., Kanevskiy, M., Marchenko, S., 2010. Resilience and vulnerability of permafrost to climate changethis article is one of a selection of papers from the dynamics of change in alaska's boreal forests: Resilience and vulnerability in response to climate warming. Canadian Journal of Forest Research 40, 1219–1236. doi:10.1139/x10-060.

Jorgenson, M.T., Shur, Y., 2007. Evolution of lakes and basins in northern alaska and discussion of the thaw lake cycle. Journal of Geophysical Research 112. doi:10.1029/2006jf000531.

Kanevskiy, M., Shur, Y., Jorgenson, M., Ping, C.L., Michaelson, G., Fortier, D., Stephani, E., Dillon, M., Tumskoy, V., 2013. Ground ice in the upper permafrost of the beaufort sea coast of alaska. Cold Regions Science and Technology 85, 56–70. doi:10.1016/j.coldregions.2012.08.002.

Kern, M., Cullen, R., Berruti, B., Bouffard, J., Casal, T., Drinkwater, M.R., Gabriele, A., Lecuyot, A., Ludwig, M., Midthassel, R., Navas Traver, I., Parrinello, T., Ressler, G., Andersson, E., Martin-Puig, C., Andersen, O., Bartsch, A., Farrell, S., Fleury, S., Gascoin, S., Guillot, A., Humbert, A., Rinne, E., Shepherd, A., van den Broeke, M.R., Yackel, J., 2020. The copernicus polar ice and snow topography altimeter (cristal) high-priority candidate mission. The Cryosphere 14, 2235–2251. doi:10.5194/tc-14-2235-2020.

Kessler, M.A., Plug, L.J., Walter Anthony, K.M., 2012. Simulating the decadal- to millennial-scale dynamics of morphology and sequestered carbon mobilization of two thermokarst lakes in nw alaska. Journal of Geophysical Research: Biogeosciences 117. doi:10.1029/2011jg001796.

Kumpula, T., Forbes, B.C., Stammler, F., Meschtyb, N., 2012. Dynamics of a coupled system: Multi-resolution remote sensing in assessing social-ecological responses during 25 years of gas field development in arctic russia. Remote Sensing 4, 1046–1068. doi:10.3390/rs4041046.

Kumpula, T., Pajunen, A., Kaarlejärvi, E., Forbes, B.C., Stammler, F., 2011. Land use and land cover change in arctic russia: Ecological and social implications of industrial development. Global Environmental Change 21, 550–562. doi:10.1016/j.gloenvcha.2010.12.010.

Lanaras, C., Bioucas-Dias, J., Galliani, S., Baltsavias, E., Schindler, K., 2018. Super-resolution of Sentinel-2 images: Learning a globally applicable deep neural network. ISPRS Journal of Photogrammetry and Remote Sensing 146, 305–319. doi:10.1016/j.isprsjprs.2018.09.018.

Lantz, T.C., 2017. Vegetation succession and environmental conditions following catastrophic lake drainage in old crow flats, yukon. ARCTIC 70, 177. doi:10.14430/arctic4646.

Lantz, T.C., Zhang, Y., Kokelj, S.V., 2022. Impacts of ecological succession and climate warming on permafrost aggradation in drained lake basins of the tuktoyaktuk coastlands, northwest territories, canada. Permafrost and Periglacial Processes 33, 176–192. doi:10.1002/ppp.2143.

Lara, M.J., Chipman, M.L., 2021. Periglacial lake origin influences the likelihood of lake drainage in northern alaska. Remote Sensing 13, 852. doi:10.3390/rs13050852.

Leibman, M., Khomutov, A., Gubarkov, A., Mullanurov, D., Dvornikov, Y., 2015. The research station "Vaskiny Dachi", Central Yamal, West Siberia, Russia - a review of 25 years of permafrost studies. Fennia – International Journal of Geography doi:10.11143/45201.

Lenton, T.M., Held, H., Kriegler, E., Hall, J.W., Lucht, W., Rahmstorf, S., Schellnhuber, H.J., 2008. Tipping elements in the earth's climate system. Proceedings of the National Academy of Sciences 105, 1786–1793. doi:10.1073/pnas.0705414105.

Li, C., Wei, Y., Liu, Y., Li, L., Peng, L., Chen, J., Liu, L., Dou, T., Wu, X., 2022. Active layer thickness in the northern hemisphere: Changes from 2000 to 2018 and future simulations. Journal of Geophysical Research: Atmospheres 127. doi:10.1029/2022jd036785.

Liu, A., Chen, Y., Cheng, X., 2023a. Effects of thermokarst lake drainage on localized vegetation greening in the yamal–gydan tundra ecoregion. Remote Sensing 15, 4561. doi:10.3390/rs15184561.

Liu, C., Xu, X., Feng, X., Cheng, X., Liu, C., Huang, H., 2023b. CALC-2020: a new baseline land cover map at 10 m resolution for the circumpolar arctic. Earth System Science Data 15, 133–153. doi:10.5194/essd-15-133-2023.

Loiko, S., Klimova, N., Kuzmina, D., Pokrovsky, O., 2020. Lake drainage in permafrost regions produces variable plant communities of high biomass and productivity. Plants 9, 867. doi:10.3390/plants9070867.

Magnússon, R.Í., Limpens, J., van Huissteden, J., Kleijn, D., Maximov, T.C., Rotbarth, R., Sass-Klaassen, U., Heijmans, M.M.P.D., 2020. Rapid vegetation succession and coupled permafrost dynamics in arctic thaw ponds in the siberian lowland tundra. Journal of Geophysical Research: Biogeosciences 125. doi:10.1029/2019jg005618.

Manasypov, R.M., Lim, A.G., Krickov, I.V., Shirokova, L.S., Shevchenko, V.P., Aliev, R.A., Karlsson, J., Pokrovsky, O.S., 2022. Carbon storage and burial in thermokarst lakes of permafrost peatlands. Biogeochemistry 159, 69–86. doi:10.1007/s10533-022-00914-y.

Masolele, R.N., Sy, V.D., Herold, M., Marcos, D., Verbesselt, J., Gieseke, F., Mullissa, A.G., Martius, C., 2021. Spatial and temporal deep learning methods for deriving land-use following deforestation: A pan-tropical case study using landsat time series. Remote Sensing of Environment 264, 112600. doi:10.1016/j.rse.2021.112600.

Meredith, M., Sommerkorn, M., Cassotta, S., Derksen, C., Ekaykin, A., Hollowed, A., Kofinas, G., Mackintosh, A., Melbourne-Thomas, J., Muelbert, M., Ottersen, G., Pritchard, H., Schuur, E., 2022. IPCC Special Report on the Ocean and Cryosphere in a Changing Climate. Cambridge University Press. chapter 1. pp. 203–320. doi:10.1017/9781009157964.005.

Moreira, A., Prats-Iraola, P., Younis, M., Krieger, G., Hajnsek, I., Papathanassiou, K.P., 2013. A tutorial on synthetic aperture radar. IEEE Geoscience and Remote Sensing Magazine 1, 6–43. doi:10.1109/mgrs.2013.2248301.

Nitze, I., 2018. Trends of land surface change from landsat time-series 1999-2014. doi:10.1594/PANGAEA.884137.

Nitze, I., Grosse, G., Jones, B., Arp, C., Ulrich, M., Fedorov, A., Veremeeva, A., 2017. Landsat-based trend analysis of lake dynamics across northern permafrost regions. Remote Sensing 9, 640. doi:10.3390/rs9070640.

Nitze, I., Grosse, G., Jones, B.M., Romanovsky, V.E., Boike, J., 2018. Remote sensing quantifies widespread abundance of permafrost region disturbances across the arctic and subarctic, datasets. doi:10.1594/PANGAEA.894755.

Obu, J., Westermann, S., Barboux, C., Bartsch, A., Delaloye, R., Grosse, G., Heim, B., Hugelius, G., Irrgang, A., Kääb, A.M., Kroisleitner, C., Matthes, H., Nitze, I., Pellet, C., Seifert, F.M., Strozzi, T., Wegmüller, U., Wieczorek, M., Wiesmann, A., 2021. Esa permafrost climate change initiative (permafrost cci): Permafrost extent for the northern hemisphere, v3.0. doi:10.5285/6E2091CB0C8B4106921B63CD5357C97C.

Olsson, P.Q., Sturm, M., Racine, C.H., Romanovsky, V., Liston, G.E., 2003. Five stages of the alaskan arctic cold season with ecosystem implications. Arctic, Antarctic, and Alpine Research 35, 74–81. doi:10.1657/1523-0430(2003)035[0074:fsotaa]2.0.co;2.

Osterkamp, T., Payne, M., 1981. Estimates of permafrost thickness from well logs in northern alaska. Cold Regions Science and Technology 5, 13–27. doi:10.1016/0165-232x(81)90037-9.

Pahlevan, N., Sarkar, S., Franz, B., Balasubramanian, S., He, J., 2017. Sentinel-2 multispectral instrument (msi) data processing for aquatic science applications: Demonstrations and validations. Remote Sensing of Environment 201, 47–56. doi:10.1016/j.rse.2017.08.033.

Pardo, J., Cernicharo, J., Serabyn, E., 2001. Atmospheric transmission at microwaves (atm): an improved model for millimeter/submillimeter applications. IEEE Transactions on Antennas and Propagation 49, 1683–1694. doi:10.1109/8.982447.

Parsekian, A.D., Grosse, G., Walbrecker, J.O., Müller-Petke, M., Keating, K., Liu, L., Jones, B.M., Knight, R., 2013. Detecting unfrozen sediments below thermokarst lakes with surface nuclear magnetic resonance. Geophysical Research Letters 40, 535–540. doi:10.1002/grl.50137.

Paull, C.K., Dallimore, S.R., Jin, Y.K., Caress, D.W., Lundsten, E., Gwiazda, R., Anderson, K., Hughes Clarke, J., Youngblut, S., Melling, H., 2022. Rapid seafloor changes associated with the degradation of arctic submarine permafrost. Proceedings of the National Academy of Sciences 119. doi:10.1073/pnas.2119105119.

Rantanen, M., Karpechko, A.Y., Lipponen, A., Nordling, K., Hyvärinen, O., Ruosteenoja, K., Vihma, T., Laaksonen, A., 2022. The arctic has warmed nearly four times faster than the globe since 1979. Communications Earth and Environment 3. doi:10.1038/s43247-022-00498-3.

Raynolds, M.K., Walker, D.A., Balser, A., Bay, C., Campbell, M., Cherosov, M.M., Daniëls, F.J., Eidesen, P.B., Ermokhina, K.A., Frost, G.V., Jedrzejek, B., Jorgenson, M.T., Kennedy, B.E., Kholod, S.S., Lavrinenko, I.A., Lavrinenko, O.V., Magnússon, B., Matveyeva, N.V., Metúsalemsson, S., Nilsen, L., Olthof, I., Pospelov, I.N., Pospelova, E.B., Pouliot, D., Razzhivin, V., Schaepman-Strub, G., Šibík, J., Telyatnikov, M.Y., Troeva, E., 2019. A raster version of the circumpolar arctic vegetation map (CAVM). Raynolds2019 232, 111297. doi:10.1016/j.rse.2019.111297.

Richards, J.A., 2009. Remote Sensing With Imaging Radar. Springer. ISBN: 97836420201935.

Romanovsky, V.E., Drozdov, D.S., Oberman, N.G., Malkova, G.V., Kholodov, A.L., Marchenko, S.S., Moskalenko, N.G., Sergeev, D.O., Ukraintseva, N.G., Abramov, A.A., Gilichinsky, D.A., Vasiliev, A.A., 2010. Thermal state of permafrost in russia. Permafrost and Periglacial Processes 21, 136–155. doi:10.1002/ppp.683.

Runge, A., Nitze, I., Grosse, G., 2022. Remote sensing annual dynamics of rapid permafrost thaw disturbances with landtrendr. Remote Sensing of Environment 268, 112752. doi:10.1016/j.rse.2021.112752.

Rutledge, K., McDaniel, M., Teng, S., Hall, H., Ramroop, T., Sprout, E., Hunt, J., Boudreau, D., Costa, H., 2023. Permafrost. URL: https://education.nationalgeographic.org/resource/permafrost/.

Schubert, G., 2015. Treatise on Geophysics, Second Edition. Elsevier. ISBN: 9780444538031.

Schuur, E.A., Abbott, B.W., Commane, R., Ernakovich, J., Euskirchen, E., Hugelius, G., Grosse, G., Jones, M., Koven, C., Leshyk, V., Lawrence, D., Loranty, M.M., Mauritz, M., Olefeldt, D., Natali, S., Rodenhizer, H., Salmon, V., Schädel, C., Strauss, J., Treat, C., Turetsky, M., 2022. Permafrost and climate change: Carbon cycle feedbacks from the warming arctic. Annual Review of Environment and Resources 47, 343–371. doi:10.1146/annurev-environ-012220-011847.

Shur, Y., Jorgenson, M.T., Kanevskiy, M.Z., 2011. Permafrost. Springer Netherlands. chapter 1. pp. 841–848. doi:10.1007/978-90-481-2642-2_400.

van der Sluijs, J., Kokelj, S., Fraser, R., Tunnicliffe, J., Lacelle, D., 2018. Permafrost terrain dynamics and infrastructure impacts revealed by uav photogrammetry and thermal imaging. Remote Sensing 10, 1734. doi:10.3390/rs10111734.

Smith, S.L., O'Neill, H.B., Isaksen, K., Noetzli, J., Romanovsky, V.E., 2022. The changing thermal state of permafrost. Nature Reviews Earth and Environment 3. doi:10.1038/s43017-021-00240-1.

Strozzi, T., Antonova, S., Günther, F., Mätzler, E., Vieira, G., Wegmüller, U., Westermann, S., Bartsch, A., 2018. Sentinel-1 sar interferometry for surface deformation monitoring in low-land permafrost areas. Remote Sensing 10, 1360. doi:10.3390/rs10091360.

Swanson, D.K., 2022. Permafrost and draining lakes in arctic alaska. Frontiers for Young Minds 10. doi:10.3389/frym.2022.692218.

T. Kumpula, B.F., Stammler, F., 2010). Remote sensing and local knowledge of hydrocarbon exploitation: The case of bovanenkovo, yamal peninsula, west siberia, russia. Arctic Institute of North America 63, 165–178.

Tanguy, R., Whalen, D., Prates, G., Pina, P., Freitas, P., Bergstedt, H., Vieira, G., 2023. Permafrost degradation in the ice-wedge tundra terrace of paulatuk peninsula (darnley bay, canada). Geomorphology 435, 108754. doi:10.1016/j.geomorph.2023.108754.

Thies, B., Bendix, J., 2011. Satellite based remote sensing of weather and climate: recent achievements and future perspectives. Meteorological Applications 18, 262–295. doi:10.1002/met.288.

Townshend, J., Short, N.M., 1984. The landsat tutorial workbook: Basics of satellite remote sensing. The Geographical Journal 150, 283. doi:10.2307/635039.

Tucker, C.J., 1979. Red and photographic infrared linear combinations for monitoring vegetation. Remote Sensing of Environment 8, 127–150. doi:10.1016/0034-4257(79)90013-0.

Ueno, S., Kawata, Y., Kusaka, T., Haba, Y., 1982. Correction of atmospheric effects on landsat mss data. Journal of remote sensing 2, 55–77. URL: https://api.semanticscholar.org/CorpusID:125828952.

Ueno, S., Mukai, S., 1977. Atmospheric effects on remotely sensed data from space. IFAC Proceedings Volumes 10, 423–428. doi:10.1016/s1474-6670(17)66865-4.

Vincent, W.F., Lemay, M., Allard, M., 2017. Arctic permafrost landscapes in transition: towards an integrated earth system approach. Arctic Science 3, 39–64. doi:10.1139/as-2016-0027.

Walker, D.A., Raynolds, M.K., Daniëls, F.J., Einarsson, E., Elvebakk, A., Gould, W.A., Katenin, A.E., Kholod, S.S., Markon, C.J., Melnikov, E.S., Moskalenko, N.G., Talbot, S.S., Yurtsev, B.A., other members of the CAVM Team, T., 2005. The circumpolar arctic vegetation map. Journal of Vegetation Science 16, 267–282. doi:10.1111/j.1654-1103.2005.tb02365.x.

Wang, C., Guo, D., Zang, S., 2023. Thermal remote sensing for mapping the sub-arctic permafrost and refining its southern limits. International Journal of Applied Earth Observation and Geoinformation 118, 103235. doi:10.1016/j.jag.2023.103235.

Webb, E.E., Liljedahl, A.K., Cordeiro, J.A., Loranty, M.M., Witharana, C., Lichstein, J.W., 2022. Permafrost thaw drives surface water decline across lake-rich regions of the arctic. Nature Climate Change 12, 841–846. doi:10.1038/s41558-022-01455-w.

Widhalm, B., Bartsch, A., Siewert, M.B., Hugelius, G., Elberling, B., Leibman, M., Dvornikov, Y., Khomutov, A., 2016. Site scale wetness classification of tundra regions with c-band sar satellite data. Proceedings of the ESA Living Planet Symposium .

Yang, J., Gong, P., Fu, R., Zhang, M., Chen, J., Liang, S., Xu, B., Shi, J., Dickinson, R., 2013. The role of satellite remote sensing in climate change studies. Nature Climate Change 3, 875–883. doi:10.1038/nclimate1908.

Zhang, T., 2005. Influence of the seasonal snow cover on the ground thermal regime: An overview. Reviews of Geophysics 43. doi:10.1029/2004rg000157.

Zhao, S., Liu, M., Tao, M., Zhou, W., Lu, X., Xiong, Y., Li, F., Wang, Q., 2023. The role of satellite remote sensing in mitigating and adapting to global climate change. Science of The Total Environment 904, 166820. doi:10.1016/j.scitotenv.2023.166820.